A Finite-Volume/Front-Tracking Method for Computations of Multiphase Flows in Complex Geometries

by

Arif Doruk Kayaalp

A Thesis Submitted to the
Graduate School of Engineering
in Partial Fulfillment of the Requirements for
the Degree of

Master of Science

in

Mechanical Engineering

Koç University

June, 2004

Koç University

Graduate School of Sciences and Engineering

This is to certify that I have examined this copy of a master's thesis by

Arif Doruk Kayaalp

and have found that it is complete and satisfactory in all respects,
and that any and all revisions required by the final
examining committee have been made.

Committee Members:

Assistant Prof. Metin Muradoğlu (Advisor)

Assistant Prof. Alper Tunga Erdoğan

Assistant Prof. Murat Sözer

Date: 22/06/2004

To my Family

ABSTRACT*

A finite-volume/front-tracking (FV/FT) method is developed for computations of multiphase flows in complex geometries. The method is based on the one field formulation of the flow equations and treating different phases as a single fluid with variable material properties. The FV method is based on the concept of dual time stepping and is combined with the front-tracking methodology. An alternating direction implicit scheme is used to integrate the flow equations in pseudo time and several convergence acceleration techniques such as preconditioning, local time-stepping and multigrid methods are used to accelerate the convergence of the sub-iterations in the FV algorithm. The interface is represented by connected Lagrangian marker points. A novel tracking algorithm is developed to track the position of front marker points in curvilinear grids and is found to be very robust and computationally efficient. The method is implemented to solve two-dimensional (plane or axisymmetric) dispersed multiphase flows and is validated for a vibrating drop problem, buoyancy-driven falling drops in a in a straight tube and the motion of buoyancy-driven drops in a periodically constricted tube.

Keywords: A finite-volume/front-tracking method, Dual time-stepping, Dispersed multiphase flows, Complex geometries

---

*Submitted to Journal of Computational Physics

ACKNOWLEDGMENTS

I would like to thank, first and foremost, my advisor, Assistant Prof. Metin Muradoğlu for his guidance and support throughout my graduate study and during the completion of this thesis. I am extremely grateful to, Assistant Prof. Murat Sözer and Assistant Prof. Alper Tunga Erdoğan, for their participation in my thesis committie and for the critical reading of my thesis.

Also, I would like to thank all my friends at Koç University who made the two years an enjoyable period of time; my research group friends in particular Bahadır; my grad student friends and all the people who surrounded me all the time in the last two years especially Irem.

Last, I would like to thank my parents Nimet Kayaalp, Arif Kayaalp and my sister Damla Kayaalp for their love, affection and support throughout my life, without their encouragement I wouldn't be what I am today. I am very fortunate to be a part of such an affectionate family.

TABLE OF CONTENTS

LIST OF TABLES

LIST OF FIGURES

NOMENCLATURE

A	amplitude of corrugation
ADI	Alternating Direction Implicit
Ca	Capillary number
CIP	Constrained Interpolation Profile
d	length scale
D	drop diameter
Δt	real-time step
$\Delta\rho$	density difference between the drop and the ambient fluids
$\Delta\tau$	pseudo-time step
Eo	Eötvös number
FD-FT	Finite Difference Front Tracking
FV-FT	Finite Volume Front Tracking
g_z	gravitational acceleration
γ	ratio of the dimensionless drop to the ambient fluid densities
h	wavelength of corrugation
κ	dimensionless drop size
κ_c	twice of the mean curvature
λ	ratio of the dimensionless drop to the ambient fluid viscosities
μ_d	viscosity of the drop
ν	kinematic viscosity of the drop fluid
Oh_d	Ohnesorge number
p	pressure
PDF	Probability Density Function
r and z	radial and axial coordinates
R	radius of the tube
Re	Reynolds number

ρ_o	density of the ambient fluid
ρ_d	density of the drop
σ	surface tension coefficient
t	physical time
τ	pseudo time
τ_{rr}, τ_{zz} and τ_{zr}	viscous stresses
θ	level of implicitness
U	velocity scale
v_r and v_z	velocity components in r and z coordinate directions
VOF	Volume-of-Fluid
ζ	magnitude of perturbation
$\mathbf{x}_f$	location of the front

Chapter 1

INTRODUCTION

Modeling of multiphase flows in complex geometries is of great importance in many engineering applications and natural processes. Both the physical modeling and the numerical computation of multiphase flows are associated with certain difficulties. These difficulties mainly arise from the existence of the moving interfaces separating the phases and immiscible fluids. In general, the geometry of the interfaces and the spatial distribution of the phases are not known as priori but are a part of the solution. The difficulties in modeling concern the physical transfer processes taking place across the interface such as momentum and phase change. The numerical difficulties arise from the fact that interface is moving and certain quantities are discontinuous across the interface, e.g., the density, viscosity and pressure.

First a short description of several terms relevant to multiphase flows will be given. A phase is a thermodynamic definition of matter, which can be either solid, liquid or gas. In a multiphase flow several phases flow together. These phases may consist of one chemical component, e.g., flow of water and water vapor (steam), or of several chemical components, e.g., flow of oil and water. Within the general multiphase terminology a phase is classified as continuous if it occupies continuously connected regions of space and is classified as disperse when it occupies disconnected regions of space. The disperse phase is formed by particles. In the sequel, particle can mean either a rigid (solid) particle or a fluid particle. Fluid particles formed by a gas phase are denoted as bubbles, while fluid particles formed by a liquid phase are called drops.

Any fluid motion originates from forces acting on fluid elements. A proper way to identify the dominant forces and those forces that may be neglected is provided by dimensionless groups, expressing the ratio between two forces. Four dimensionless groups, Reynolds number Re, Eötvös number Eo (interchangeably called the Bond number, Bo), the Ohne-

sorge number Oh_d, and the Capillary number Ca are important to mention. The Reynolds, Eötvös, Ohnesorge, and Capillary numbers represent the ratios between inertial and viscous forces, the buoyancy and surface tension forces, the viscous and inertial forces multiplied by the surface tension forces and the viscous and surface tension forces, respectively, and are defined as

$$\begin{aligned} Re &= \frac{\rho_d d U}{\mu_d}, \\ E_o &= \frac{g_z \Delta\rho d^2}{\sigma}, \\ Oh_d &= \frac{\mu_d}{\sqrt{\rho_d d \sigma}}, \\ Ca &= \frac{\mu_d U}{\sigma}, \end{aligned} \tag{1.1}$$

where ρ_d, and μ_d denote the density and viscosity of the drop fluid; ρ_o, and μ_o denote the density and viscosity of the ambient fluid; $\Delta\rho = \rho_d - \rho_o$ and σ denote the density difference between the drop and the ambient fluids, and the surface tension coefficient; g_z, U and d denote the gravitational acceleration, the velocity and length scales, respectively. The parameters that govern the motion of a freely suspended liquid drop through a capillary at low Reynolds number are the size of the drop relative to the diameter of the tube, the ratio of the viscosity of the drop fluid to the viscosity of the ambient fluid, and the capillary number, as mentioned above. These three parameters also affect the relative mobilities of fluid phases in flow through porous media, but the capillary number holds special significance because it determines whether trapped drops can be mobilized and displaced through constrictions.

Especially, the motion of immiscible liquid drops and bubbles suspended in low Reynolds number flow through a capillary tube is a prototype problem that has proven useful in analyzing multiphase fluid systems in a variety of flows [6, 26, 30]. A prominent example is multiphase flow in porous media, which is relevant to oil recovery methods that use liquids, gases, and foams to displace oil drops trapped within the pores of rock formations. Studies of the motion of drops and bubbles in capillaries provide insight into pore-scale hydrodynamics that cannot be scrutinized in practice. In the context of biomechanics it is known that the alteration of the blood flow by the presence of stenoses on the vessel walls is closely related to vascular diseases [6].

The presence of deforming phases makes the multiphase flow computations a challenging problem and strong interactions between the phases and complex boundaries add further complexity to the problem. Therefore, the progress was rather slow and the computations of multiphase flows have been usually restricted to simple geometries and boundary conditions. Since nearly all multiphase flows of practical interest involve complex geometries and boundary conditions, it is of obvious interest to extend the modeling and computational techniques to treat multiphase flows in complex geometries.

The interaction of droplets with the geometry in which they are constrained to traverse motion has received some attention from numerical (Tsai and Miksis [30], Manga [14], Udaykumar et al. [31]) and experimental viewpoints (Olbricht and Leal[17], Hemmat and Borhan [8]). Since the major focus has been on the behavior of multiphase flow through porous media with applications in oil recovery, such flows have been restricted to the creeping flow regime. The boundary integral technique was applied to simulate such a problem by Tsai and Miksis [30]. In a recent work, Manga [14] applied the same technique to study the behavior of drops in geometries such as a driven cavity and bifurcating channel, again restricted to Stokes flow. Udaykumar et al. [31] studied the deformation of droplets in viscosity and inertia dominated flows through a constricted tube and reproduced the results obtained by Tsai and Miksis [30].

A number of experimental studies have examined the motion of liquid droplets through sinusoidally constricted capillary tubes, however the most relevant ones have been performed by Olbricht and Leal [17] and Hemmat and Borhan [8]. Olbricht and Leal [17] considered the pressure driven motion of immiscible neutrally-buoyant drops in pressure driven flow through horizontal capillaries whose diameter changes periodically with the axial position. They measured the average drop speed and correlated those values with the observed time-dependant drop shapes. Their results were mainly qualitative and they demonstrated the effect of capillary geometry on the shape and mobility of drops. Hemmat and Borhan [8] reported the buoyancy driven motion of viscous drops and gas bubbles through a vertical capillary with periodic variations in order to examine the effect of capillary geometry on drop deformation and breakup.

Simulation of multiphase flows is notoriously difficult mainly due to the presence of deforming phase boundaries. A variety of numerical methods have been developed and success-

fully applied to a wide range of multifluid and multiphase flow problems [19, 24, 25, 28, 33]. In spite of this success, significant progress is still needed especially for accurate computations of multiphase flows involving strong interactions with complex solid boundaries.

The most popular approaches to compute the multiphase flows are classified into four categories: The first category is the front capturing method such as the Volume-Of-Fluid (VOF) [9, 24] and the level-set [19, 25, 27] methods. In these methods, the front is captured indirectly through the volume-fraction distribution (VOF) or the zero-level-set of the distance function. The constrained interpolation profile (CIP) method of Yabe [33] also belongs to this category. Traditionally, the main difficulty in using these methods has been the maintenance of a sharp boundary between the different fluids and the computation of the surface tension. The second class of methods, and the one that offers the potentially highest accuracy, uses separate, boundary fitted grids for each phase. The steady rise of buoyant, deformable, axisymmetric bubbles was simulated by Ryskin and Leal [23] using this method. This method is best suited for relatively simple geometries, and applications to complex fully three-dimensional problems with unsteady deforming phase boundaries are very rare. The third class is the Lagrangian methods with moving grids [10]. The fourth approach used in the present study is the front-tracking method [28, 32]. The front-tracking method developed by Unverdi and Tryggvason [32] is based on the one-field formulation of the Navier-Stokes equations and treating different phases as a single fluid with variable material properties. In this approach, a stationary Eulerian grid is used for the fluid flow and the interface is tracked explicitly by a separate Lagrangian grid. The immersed boundary method developed by Peskin [20] is used to smoothly discretize the jumps in material properties and to treat the effects of surface tension. The front-tracking method combined with a finite-difference flow solver has been successfully applied to a wide range of multiphase flow problems but almost all in relatively simple geometries [28] except for Udaykumar et al. [31]. Udaykumar et al. [31] used a mixed Eulerian-Lagrangian algorithm to compute flows in arbitrary geometries. The front tracking method has been reviewed recently by Tryggvason et al. [28].

It is of great importance to be able to accurately model strong interactions between bubbles/drops and the curved solid boundary in many engineering and scientific applications such as microfluidic systems [26], pore-scale multi-phase flow processes [17, 18] and biological

systems [6, 21]. The front-tracking method has many advantages such as its simplicity and lack of numerical diffusion. However, its main disadvantage is probably the difficulty to maintain the communication between the Lagrangian marker points and Eulerian body-fitted curvilinear or unstructured grids. In the present study, a finite-volume/front-tracking method is developed to compute dispersed multiphase flows in complex geometries using body-fitted curvilinear grids. An efficient and robust tracking algorithm is developed for tracking the front marker points in body-fitted curvilinear grids. The tracking algorithm utilizes an auxiliary regular Cartesian grid and it can be easily extended to unstructured grids. The front-tracking methodology is extended to body-fitted curvilinear grids and is combined with a newly developed finite-volume method to facilitate accurate and efficient modeling of strong interactions between the phases and complex solid boundary. The finite-volume method is based on the concept of dual (or pseudo) time-stepping method and is developed for time-accurate computations of incompressible laminar flows. The dual time-stepping method uses sub-iterations in pseudo time and has a number of advantages. It directly couples the continuity and momentum equations for incompressible flows and eliminates the factorization error in factored implicit schemes. Also, it eliminates the errors due to approximations made in the implicit operator to improve numerical efficiency and errors due to lagged boundary conditions at the solid and internal fluid boundaries. Finally, it brings out the ability to use non-physical, preconditioned iterative methods for more efficient convergence of the sub-iterations [4].

In order for the implicit method to be an effective smoothing algorithm when used in conjunction with the multigrid algorithm, it is important to include an accurate representation of the numerical dissipation terms. These usually include fourth order differences of the solution in order to maintain high accuracy, and their inclusion in the implicit operator requires the solution of pentadiagonal systems of equations for each one-dimensional factor. The addition of the numerical dissipation terms and the details of the pentadiagonal system are presented in the appendices. Block ADI methods for the equations of compressible gas dynamics were first introduced by Briley and McDonald [2] and by Beam and Warming [1]. The basis of these methods is to approximate the spatial derivatives as weighted averages of differences taken at the old and new time step levels, linearizing the changes in the flux vectors using Taylor series expansions in time, and then to approximate the implicit oper-

ator as a product of one-dimensional factors [3]. An efficient diagonalized ADI method of this sort has been developed by Caughey [3], who applied the scheme to compute transonic flows past airfoils.

The present FV-FT method is implemented for computations of two dimensional (plane or axisymmetric) dispersed multiphase flows in complex geometries. Two-dimensional results have been published earlier in [16] by Muradoglu and Gokaltun, and axisymmetric flow cases are presented in this thesis. Some results presented here are also included in [12] by Muradoglu and Kayaalp.

The thesis is organized into three main parts. In Chapter 2, the governing equations are briefly reviewed and are transformed into an arbitrary curvilinear coordinate system. The finite-volume/front-tracking algorithm is described, with details presented in the Appendices. Chapter 3 validates the numerical method for three test cases. The method is first tested for an oscillating drop and the results are compared with the analytical solutions. The method is then applied to compute the motion of the drops falling due to gravity in a straight channel studied earlier numerically by Han and Tryggvason [7]. It is found that the present results are in very good agreement with the results obtained by Han and Tryggvason [7]. In the third test case the method is applied to buoyancy driven motion of drops in constricted channels studied experimentally by Hemmat and Borhan [8]. Finally, some conclusions are drawn in Chapter 5.

Chapter 2

NUMERICAL METHOD

In this chapter, the governing equations are briefly reviewed and transformed into an arbitrary curvilinear coordinate system. Then the finite-volume/front-tracking algorithm is described in detail.

2.1 Mathematical Formulation

The incompressible flow equations for an axisymmetric flow can be written in the cylindrical coordinates in the vector form as

$$\frac{\partial \mathbf{q}}{\partial t}+\frac{\partial \mathbf{f}}{\partial r}+\frac{\partial \mathbf{g}}{\partial z}=\frac{\partial \mathbf{f}_v}{\partial r}+\frac{\partial \mathbf{g}_v}{\partial z}+\mathbf{h}_v+\mathbf{f}_b, \tag{2.1}$$

where

$$\mathbf{q}=\left\{\begin{array}{c} 0 \\ r\rho v_r \\ r\rho v_z \end{array}\right\}, \quad \mathbf{f}=\left\{\begin{array}{c} rv_r \\ r(\rho v_r^2+p) \\ r\rho v_r v_z \end{array}\right\}, \quad \mathbf{g}=\left\{\begin{array}{c} rv_z \\ r\rho v_r v_z \\ r(\rho v_z^2+p) \end{array}\right\}, \tag{2.2}$$

and

$$\mathbf{f}_v=\left\{\begin{array}{c} 0 \\ \tau_{rr} \\ \tau_{zr} \end{array}\right\}, \quad \mathbf{g}_v=\left\{\begin{array}{c} 0 \\ \tau_{zr} \\ \tau_{zz} \end{array}\right\}, \quad \mathbf{h}_v=\left\{\begin{array}{c} 0 \\ p-\frac{2}{r}\frac{\partial}{\partial r}(r\mu v_r)-\frac{\partial}{\partial z}(\mu v_z) \\ -\frac{\partial}{\partial z}(\mu v_z) \end{array}\right\}. \tag{2.3}$$

In Eqs.(2.1)-(2.3), r and z are the radial and axial coordinates and t is the physical time; ρ, μ and p are the fluid density, the dynamic viscosity and pressure; v_r and v_z are the velocity components in r and z coordinate directions, respectively. The elements of the viscous stresses appearing in the viscous flux vectors are given by

$$\tau_{rr}=2\mu\frac{\partial(rv_r)}{\partial r}, \quad \tau_{zz}=2\mu\frac{\partial(rv_z)}{\partial z}, \quad \tau_{zr}=\mu\left(\frac{\partial(rv_r)}{\partial z}+\frac{\partial(rv_z)}{\partial r}\right). \tag{2.4}$$

The last term in Eq.(2.1) represents the body forces resulting from the buoyancy and surface tension and is given by

$$\mathbf{f}_b=-r(\rho_o-\rho)\mathbf{G}-\int_S r\sigma\kappa\mathbf{n}\delta(\mathbf{x}-\mathbf{x}^f)ds, \tag{2.5}$$

where the first term represents the body force due to buoyancy with ρ_o and $\mathbf{G}$ being the density of ambient fluid and the gravitational acceleration, respectively. The second term in Eq.(2.5) represents the body force due to the surface tension, and δ, $\mathbf{x}_f$, σ, κ_c, $\mathbf{n}$, S and ds denote the Dirac delta function, the location of the front, the surface tension coefficient, the twice of the mean curvature, the outward unit normal vector on the interface, the surface area of the interface and the surface area element of the interface, respectively.

In Eq.(2.1), the fluids are assumed to be incompressible so that the density of a fluid particle remains constant, i.e.,

$$\frac{D\rho}{Dt} = 0, \tag{2.6}$$

where the substantial derivative is defined as $\frac{D}{Dt} = \frac{\partial}{\partial t} + \mathbf{u} \cdot \nabla$. It is also assumed that the viscosity in each fluid particle remains constant

$$\frac{D\mu}{Dt} = 0. \tag{2.7}$$

As can be seen in Eq.(2.1), the continuity equation is decoupled from the momentum equations since it does not have any time derivative term. In order to overcome this difficulty and to be able to use a time-marching solution algorithm, artificial time derivative terms are added to the flow equations in the form

$$\Gamma^{-1}\frac{\partial \mathbf{w}}{\partial \tau} + \mathbf{I}^1\frac{\partial \rho \mathbf{w}}{\partial t} + \frac{\partial \mathbf{f}}{\partial r} + \frac{\partial \mathbf{g}}{\partial z} = \frac{\partial \mathbf{f}_v}{\partial r} + \frac{\partial \mathbf{g}_v}{\partial z} + \mathbf{h}_v + \mathbf{f}_b \tag{2.8}$$

where τ is the pseudo time. The solution vector $\mathbf{w}$, the incomplete identity matrix I^1 and the preconditioning matrix Γ^{-1} are given by

$$\mathbf{w} = \begin{Bmatrix} rp \\ rv_r \\ rv_z \end{Bmatrix}, \quad I^1 = \begin{bmatrix} 0 & 0 & 0 \\ 0 & 1 & 0 \\ 0 & 0 & 1 \end{bmatrix}, \quad \Gamma^{-1} = \begin{bmatrix} \frac{1}{\rho\beta^2} & 0 & 0 \\ 0 & \rho & 0 \\ 0 & 0 & \rho \end{bmatrix}, \tag{2.9}$$

where β is the preconditioning parameter to be determined and it has dimensions of velocity. Note that the relation $\mathbf{q} = \rho I^1 \mathbf{w}$ has been used in Eq.(2.8). The analysis for the preconditioning parameter β is provided in Appendix B, and according to this analysis

$$\beta^2 = \kappa_\beta U_{\text{ref}}^2 \left[1 + \frac{1}{4Re_\ell^2}\right], \tag{2.10}$$

where κ_β is a constant of order of unity, U_{ref} and ℓ are the velocity and length scales, respectively, and the Reynolds number Re_ℓ is defined as

$$Re_\ell = \frac{\rho U_{\text{ref}} \ell}{\mu_o}. \tag{2.11}$$

Equation (2.8) can be transformed into a general, curvilinear coordinate system

$$\xi = \xi(r, z), \quad \eta = \eta(r, z), \tag{2.12}$$

and the resulting equations take the form

$$\Gamma^{-1} \frac{\partial h\mathbf{w}}{\partial \tau} + \mathbf{I}^1 \frac{\partial \rho h\mathbf{w}}{\partial t} + \frac{\partial h\mathbf{F}}{\partial \xi} + \frac{\partial h\mathbf{G}}{\partial \eta} = \frac{\partial h\mathbf{F}_v}{\partial \xi} + \frac{\partial h\mathbf{G}_v}{\partial \eta} + h(\mathbf{h}_v + \mathbf{f}_b), \tag{2.13}$$

where

$$h = r_\xi z_\eta - r_\eta z_\xi, \tag{2.14}$$

represents the Jacobian of the transformation. The vectors

$$h\mathbf{F} = z_\eta \mathbf{f} - r_\eta \mathbf{g}; \quad h\mathbf{G} = -z_\xi \mathbf{f} + r_\xi \mathbf{g}, \tag{2.15}$$

and

$$h\mathbf{F}_v = z_\eta \mathbf{f}_v - r_\eta \mathbf{g}_v; \quad h\mathbf{G}_v = -z_\xi \mathbf{f}_v + r_\xi \mathbf{g}_v, \tag{2.16}$$

represent the transformed inviscid and viscous flux vectors, respectively.

Once the material properties and surface tension forces have been determined, any standard time-marching algorithm can, in principle, be used to solve Eq. (2.13) since it is in the same form as the usual continuum flow equations. Three types of grids used in the present method are sketched in Fig 2.1. A fixed curvilinear grid is used to solve the conservation equations (Eq. (2.13)) while a Lagrangian grid of lower dimension is used to track the interface separating different phases. An auxiliary uniform Cartesian grid is used to maintain computationally efficient communication between the curvilinear and Lagrangian grids.

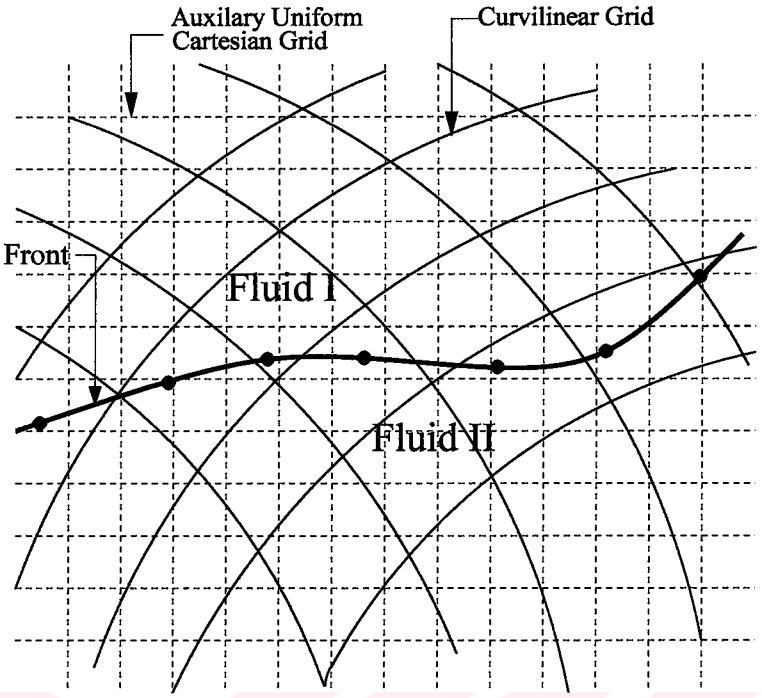

Figure 2.1: Three types of grids used in the computations. The governing equations are solved on a fixed Eulerian curvilinear grid and the interface between different phases is represented by a Lagrangian grid consisting of connected marker points. An auxiliary uniform Cartesian grid is used to maintain communication between the curvilinear and Lagrangian grids.

2.2 Integration of the Flow Equations

Following Caughey [4], a two-parameter family of numerical scheme to solve Eq.(2.13) can be written as

$$\begin{aligned}\Gamma^{-1}h\frac{\mathbf{w}^{p+1}-\mathbf{w}^{p}}{\Delta\tau} \;+\; & I^{1}h\frac{(2+\varphi)(\rho\mathbf{w})^{p+1}-2(1+\varphi)(\rho\mathbf{w})^{n}+\varphi(\rho\mathbf{w})^{n-1}}{2\Delta t}= \\ & -\;\theta\left[\frac{\partial h(\mathbf{F}-\mathbf{F}_v)}{\partial\xi}+\frac{\partial h(\mathbf{G}-\mathbf{G}_v)}{\partial\eta}\right]^{p+1}+\theta h(\mathbf{h}_v^{p}+\mathbf{f}_b^{n+1}) \\ & -\;(1-\theta)\left[\frac{\partial h(\mathbf{F}-\mathbf{F}_v)}{\partial\xi}+\frac{\partial h(\mathbf{G}-\mathbf{G}_v)}{\partial\eta}-h(\mathbf{h}_v+\mathbf{f}_b)\right]^{n}, \quad (2.17)\end{aligned}$$

where $(\cdots)^p$ and $(\cdots)^n$ denote the pseudo and physical time levels, respectively. The parameter φ governs the approximation to the physical time-derivative and θ determines the level of implicitness of the method in pseudo time. Note that when a steady state is reached in pseudo time, we have $\mathbf{w}^p \to \mathbf{w}^{n+1}$. Three combinations of φ and θ are of particular

φ	θ	Scheme	Order of accuracy
0	1	Implicit Backward Euler Method	First order
0	1/2	Implicit Trapezoidal Method	Second order
1	1	Three-Point Backward Implicit Method	Second order

Table 2.1: Physical time-integration schemes

interest and correspond to different approximations in the physical time as summarized in Table 2.1 [4]. In the present study, the three-point backward implicit method is used throughout. Note that the terms $\mathbf{h}_v$ and $\mathbf{f}_b$ are treated explicitly in the pseudo time in the present formulation although it is possible to include $\mathbf{h}_v$ into the implicit operator. The increment $\Delta\tau$ represents the time step for sub-iteration while Δt represents the physical time step which is usually different. The correction $\Delta\mathbf{w}^p = \mathbf{w}^{p+1} - \mathbf{w}^p$ is computed according to

$$\begin{aligned} h\left[\frac{\Gamma^{-1}}{\Delta\tau} + I^1\frac{(2+\varphi)}{2\Delta t}\rho^{p+1}\right]\Delta\mathbf{w}^p = &-hI^1\frac{(2+\varphi)(\rho\mathbf{w})^p - 2(1+\varphi)(\rho\mathbf{w})^n + \varphi(\rho\mathbf{w})^{n-1}}{2\Delta t} \\ &- \theta\left[\frac{\partial h(\mathbf{F}-\mathbf{F}_v)}{\partial\xi} + \frac{\partial h(\mathbf{G}-\mathbf{G}_v)}{\partial\eta}\right]^{p+1} + \theta h(\mathbf{h}_v^p + \mathbf{f}_b^{n+1}) \\ &- (1-\theta)\left[\frac{\partial h(\mathbf{F}-\mathbf{F}_v)}{\partial\xi} + \frac{\partial h(\mathbf{G}-\mathbf{G}_v)}{\partial\eta} - h(\mathbf{h}_v + \mathbf{f}_b)\right]^n. \end{aligned} \tag{2.18}$$

The sub-iteration to solve Eq.(2.18) is linearized as

$$\begin{aligned} (h\mathbf{F})^{p+1} &= (h\mathbf{F})^p + A^p\Delta\mathbf{w}^p + O(\Delta\tau^2), \\ (h\mathbf{G})^{p+1} &= (h\mathbf{G})^p + B^p\Delta\mathbf{w}^p + O(\Delta\tau^2), \\ (h\mathbf{F}_v)^{p+1} &= (h\mathbf{F}_v)^p + A_v^p\Delta\mathbf{w}_\xi^p + O(\Delta\tau^2), \\ (h\mathbf{G}_v)^{p+1} &= (h\mathbf{G}_v)^p + B_v^p\Delta\mathbf{w}_\eta^p + O(\Delta\tau^2), \end{aligned} \tag{2.19}$$

where the inviscid and viscous Jacobian matrices are defined as

$$A^p = \left\{\frac{\partial h\mathbf{F}}{\partial\mathbf{w}}\right\}^p, \quad B^p = \left\{\frac{\partial h\mathbf{G}}{\partial\mathbf{w}}\right\}^p, \quad A_v^p = \left\{\frac{\partial h\mathbf{F}_v}{\partial\mathbf{w}_\xi}\right\}^p, \quad B_v^p = \left\{\frac{\partial h\mathbf{G}_v}{\partial\mathbf{w}_\eta}\right\}^p, \tag{2.20}$$

with $\mathbf{w}_\xi = \frac{\partial\mathbf{w}}{\partial\xi}$ and $\mathbf{w}_\eta = \frac{\partial\mathbf{w}}{\partial\eta}$. A linearized approximation to Eq.(2.18) with the details presented in Appendix C can then be written as

$$h\left\{S + \frac{\theta}{h}\left(\frac{\partial}{\partial\xi}A + \frac{\partial}{\partial\eta}B - \frac{\partial}{\partial\xi}A_v\frac{\partial}{\partial\xi} - \frac{\partial}{\partial\eta}B_v\frac{\partial}{\partial\eta}\right)\right\}^p\Delta\mathbf{w}^p = -\mathbf{R}^p, \tag{2.21}$$

where

$$S = \frac{\Gamma^{-1}}{\Delta\tau} + I^1 \frac{(2+\varphi)}{2\Delta t}\rho^{p+1}, \tag{2.22}$$

and

$$\begin{aligned}\mathbf{R}^p &= hI^1 \frac{(2+\varphi)(\rho\mathbf{w})^p - 2(1+\varphi)(\rho\mathbf{w})^n + \varphi(\rho\mathbf{w})^{n-1}}{2\Delta t} \\ &+ \theta\left[\frac{\partial h(\mathbf{F}-\mathbf{F}_v)}{\partial\xi} + \frac{\partial h(\mathbf{G}-\mathbf{G}_v)}{\partial\eta} - h\mathbf{h}_v\right]^p + \theta h\mathbf{h}_b^{n+1} \\ &+ (1-\theta)\left[\frac{\partial h(\mathbf{F}-\mathbf{F}_v)}{\partial\xi} + \frac{\partial h(\mathbf{G}-\mathbf{G}_v)}{\partial\eta} - h(\mathbf{h}_v+\mathbf{f}_b)\right]^n.\end{aligned} \tag{2.23}$$

In Eq.(2.22), ρ^{p+1} is approximated as $\rho^{p+1} \cong \rho^{n+1}$ in the solution process. Equation (2.21) represents a linear system of equations that can be solved for the correction $\Delta\mathbf{w}^p$ by a variety of methods, but following Briley and McDonald [2] and Beam and Warming [1], it is factorized for computational efficiency as

$$h\left\{S + \frac{\theta}{h}\left(\frac{\partial}{\partial\xi}A - \frac{\partial}{\partial\xi}A_v\frac{\partial}{\partial\xi}\right)\right\}S^{-1}\left\{S + \frac{\theta}{h}\left(\frac{\partial}{\partial\eta}B - \frac{\partial}{\partial\eta}B_v\frac{\partial}{\partial\eta}\right)\right\}\Delta\mathbf{w}^p = -\mathbf{R}^p, \tag{2.24}$$

which can be solved in two steps using a block tridiagonal solver when the spatial derivatives are discretized by three-point approximations. The discretization of Eq.(2.21) with added artificial numerical dissipation terms and the elements of the pentadiagonal system are given in Appendix C.

The spatial derivatives are approximated using a cell-centered finite-volume method that is equivalent to second order central differences on a uniform Cartesian grid and fourth order numerical dissipation terms similar to that of Caughey [3] are added to the right hand side of Eq.(2.13) to prevent the odd-even decoupling. Note that the numerical dissipation terms are treated explicitly in pseudo time. Since the accuracy in pseudo time is not of interest, in addition to the preconditioning method, a multigrid method similar to that of Caughey [4] and a local time-stepping method are used to further accelerate the convergence rate in pseudo time.

A diagonalized version of the ADI method similar to that of Pulliam and Chaussee [22] has also been implemented in which only the convective terms are treated implicitly and all other terms are treated explicitly in pseudo time. A plane two dimensional version of the diagonalized scheme is described by Muradoglu and Gokaltun [16]. Since all the cases studied in the thesis are essentially in the Stokes' limit, it is found that block diagonal

version is more efficient than the diagonalized version. Therefore, the block diagonal version of the ADI method is used in the present study.

2.3 Tracking Algorithm

The interface between different phases are represented by a Lagrangian grid with connected marker points as shown in Fig. 2.1. The marker points can be considered as fluid particles moving with local flow velocity. In order to maintain communication between the Lagrangian and fixed curvilinear grids, it is necessary to determine the locations of the marker points in the curvilinear grid at every physical time step. Although it is a simple task to determine locations of the marker points in a uniform Cartesian mesh, it is substantially more difficult to track them in a general curvilinear or in an unstructured grid. To overcome this difficulty and to keep tracking computationally feasible, a new tracking algorithm is developed and is found to be very robust and computationally efficient. The present tracking algorithm utilizes an auxiliary uniform Cartesian grid as sketched in Fig. 2.1. The overall algorithm can be summarized as follows: At the beginning of each simulation, a uniform Cartesian grid is generated such that it covers the entire computational domain. The cell size of the uniform grid is typically taken as the half of the size of the smallest curvilinear grid cell. It is then found which uniform Cartesian grid nodes reside in each curvilinear grid cell and this information is stored in an array. Referring to the sketch in Fig. 2.2, for example, the nodal point Q is found to be in the curvilinear grid cell $ABCD$ by performing the vector operations $\vec{k} \cdot (|\overrightarrow{AB}| \times |\overrightarrow{AQ}|) \geq 0$, $\vec{k} \cdot (|\overrightarrow{BC}| \times |\overrightarrow{BQ}|) \geq 0$, $\vec{k} \cdot (|\overrightarrow{CD}| \times |\overrightarrow{CQ}|) \geq 0$, and $\vec{k} \cdot (|\overrightarrow{DA}| \times |\overrightarrow{DQ}|) \geq 0$, where $\vec{k}$ is the outward unit vector perpendicular to the cell $ABCD$. The same procedure is used for all other nodal points enclosed by the rectangle consisting of the uniform grid cells that enclose $ABCD$, i.e., the uniform grid cells in the rectangle shown by thick solid borderline in the sketch, and the entire process is repeated for all other curvilinear grid cells. It is emphasized that all these computations are done only once at the beginning of each simulation as a preprocessing. Then, in each physical time step, it is first determined where the front points reside in the uniform grid. Referring to the sketch in Fig. 2.3, for instance, it is first found that the front point P is in (I, J) cell of the uniform grid and then it is determined that the nodes of (I, J) cell reside in the curvilinear grid cells (i, j), $(i, j-1)$ and $(i-1, j-1)$ as shown by the dashed line in the

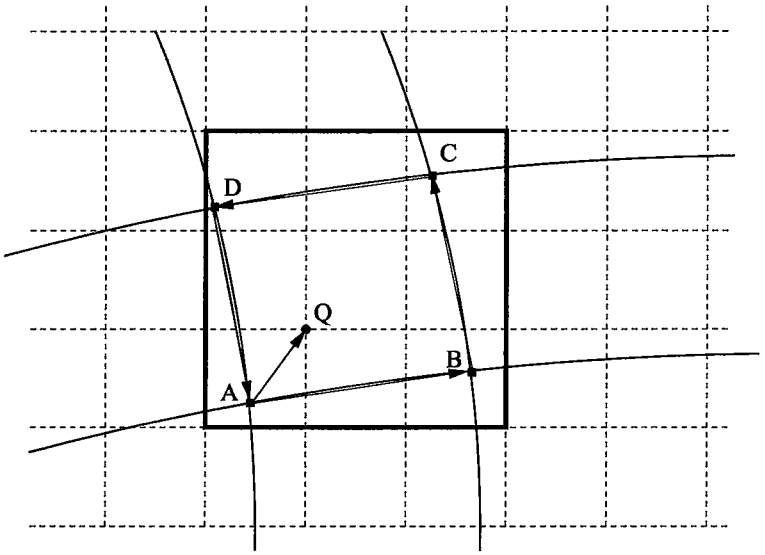

Figure 2.2: Preprocessing of the uniform Cartesian grid. Vector algebra is used to determine which uniform Cartesian grid nodes reside in each curvilinear grid cell.

sketch. As a result, we conclude that the front point P resides in the region consisting of the curvilinear grid cells $(i-1:i, j-1:j)$ and this region is expanded to include the cells $(i-2:i+1, j-2:j+1)$. Finally the cells $(i-2:i+1, j-2)$ and $(i-2, j-2:j+1)$ are eliminated based on the relative distance of their outer nodes to the point P compared to the cells $(i-2:i+1, j+1)$ and $(i+1, j-2:j+1)$, respectively. At the end of this process, it is determined that the front point P resides in the domain composed by the cells $(i-1:i+1, j-1:j+1)$. The front properties evaluated at the point P are distributed onto these cells and flow variables such as velocity field are interpolated onto point P from these cells. It is found that this tracking algorithm is very robust and computationally efficient as it essentially reduces the particle tracking in curvilinear grid to a particle tracking on a uniform grid with a look up table. Since the present tracking algorithm is general, it can also be used to track Lagrangian points in other methods such as the particle-based Monte Carlo method widely used in solving the probability density function (PDF) model equations of turbulent reacting flows [15]. In addition, it can also be adapted for unstructured grids.

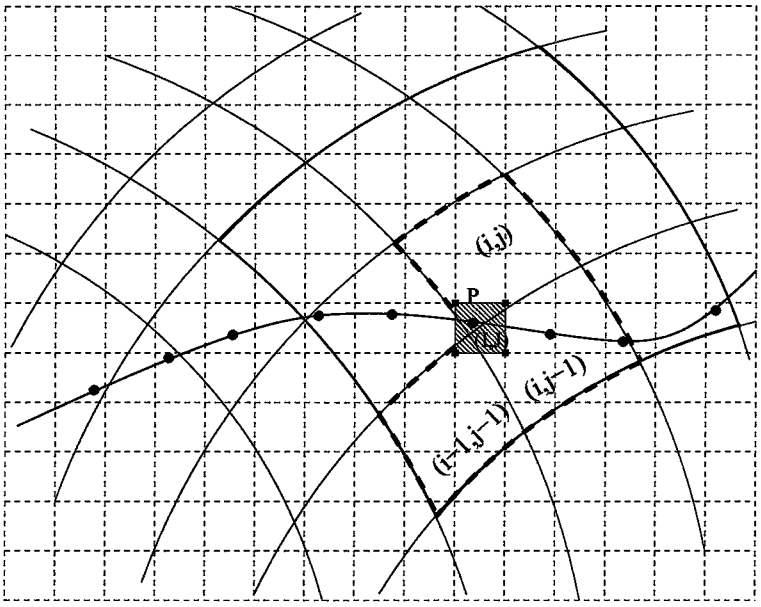

Figure 2.3: The tracking algorithm for curvilinear grids.

2.4 Smoothing the Front Properties onto the Curvilinear Grid

Since the flow equations are solved on the curvilinear grid but the surface tension is computed on the front, it is necessary to convert the surface tension into a body force by an appropriate distribution function [28]. This involves an approximation to the delta function on the curvilinear grid in a conservative manner. Let ϕ_f be an interface quantity per unit surface area, it should be converted into the grid value ϕ_g given per unit volume. To ensure that total value is conserved in the smoothing, we must have

$$\int_{\Delta s} \phi_f(s)ds = \int_{\Delta v} \phi_g(\mathbf{x})dv, \tag{2.25}$$

where Δv is the volume of the grid cell. Following Tryggvason et al. [28], this consistency condition is satisfied by writing

$$\phi_{ij} = \sum_l \phi_l w_{ij}^l \frac{\Delta s_l}{v_{ij}}, \tag{2.26}$$

where ϕ_l is a discrete approximation to the front value ϕ_f, ϕ_{ij} is an approximation to the grid value ϕ_g, Δs is the area of front element l and w_{ij}^l is the weight of grid point ij with

respect to element l. For consistency, the weights must satisfy

$$\sum_{ij} w_{ij}^{l} = 1, \tag{2.27}$$

but can be selected in different ways [28]. In the present study, the weight for the grid point ij for smoothing from $\mathbf{x}_p = (r_p, z_p)$ is defined as a tensor-product kernel in the form

$$w_{ij}(\mathbf{x}_p) = K(r_r)K(r_z), \tag{2.28}$$

where $r_r = |r_p - r_{ij}|/r_{\max}$ and $r_z = |z_p - z_{ij}|/z_{\max}$. Note that $r_{\max}$ and $z_{\max}$ are the maximum distance of the grid nodes on which the front quantity ϕ_{ij} is to be distributed in r and z directions, respectively. The functional form of K used here is

$$K(\hat{r}) = \begin{cases} \frac{4}{3} - 8(1-\hat{r})\hat{r}^2 & \text{if} \quad \hat{r} \leq 0.5 \\ \frac{8}{3}(1-\hat{r})^3 & \text{if} \quad 0.5 < \hat{r} \leq 1.0 \\ 0 & \text{otherwise,} \end{cases} \tag{2.29}$$

which is symmetric about $\hat{r} = 0$, and piecewise cubic with continuous first and second derivatives. The weights w_{ij} are normalized to satisfy the consistency condition given by Eq.(2.27). The weights w_{ij} are also used to interpolate grid values such as velocity field from the curvilinear grid onto the front points.

2.5 Computation of Material Properties

The material properties such as density and viscosity are computed according to

$$\begin{aligned} \rho &= \phi\rho_d + (1-\phi)\rho_o \\ \mu &= \phi\mu_d + (1-\phi)\mu_o, \end{aligned} \tag{2.30}$$

where the subscripts o and d refer to the ambient and the drop fluids, respectively. The indicator function ϕ is defined such that it is unity inside and zero outside of the drops and, following Tryggvason et al. [28], it is obtained by solving the Poisson equation

$$\nabla^2\phi = \nabla_h \cdot \nabla_h\phi, \tag{2.31}$$

where ∇_h is the discrete version of the gradient operator. The jump $\nabla_h\phi$ is distributed on the neighboring grid cells using the Peskin distribution [28] and Eq. (2.31) is then solved

on the uniform grid in the vicinity of each drop. After computing the indicator function on the uniform grid, it is interpolated onto the curvilinear grid using bilinear interpolations. In fact, it is possible to efficiently solve the Poisson equation on the curvilinear grid but the above procedure seems to be robust and produces sufficiently smooth solutions for the problems studied in the present work.

2.6 Surface Tension

The surface tension on each front element is computed following the procedure described by Tryggvason et al. [28]. The surface tension on a small front element can be computed as

$$\delta F_\sigma = \int_{\Delta s} r\sigma\kappa_c \mathbf{n} ds. \tag{2.32}$$

Using the definition of curvature of a two-dimensional curve, i.e., $\kappa\mathbf{n} = \partial\mathbf{s}/\partial s$ and accounting for the axisymmetry of the problem, Eq. (2.32) can be integrated to yield

$$\delta F_\sigma = r\sigma(\mathbf{s}_2 - \mathbf{s}_1) - \Delta s\sigma\mathbf{e}_r, \tag{2.33}$$

where $\mathbf{e}_r$ denotes the unit vector in the radial direction. The tangent vector to the curve $\mathbf{s}$ is computed directly by a Lagrange polynomial fit through the end-points of each element and the end-points of adjacent element in the same way as described by Tryggvason et al. [28].

2.7 The Overall Solution Procedure

The finite-volume and front-tracking methods described above are combined as follows. In advancing solutions from physical time level n ($t_n = n \cdot \Delta t$) to level $n+1$, the locations of the marker points at the new time level $n+1$ are first predicted using an explicit Euler method, i.e.,

$$\widetilde{\mathbf{X}}_p^{n+1} = \mathbf{X}_p^n + \Delta t \mathbf{V}_p^n, \tag{2.34}$$

where $\mathbf{X}_p$ and $\mathbf{V}_p$ denote the position of front marker points and the velocity interpolated from the neighboring curvilinear grid points onto the front point $\mathbf{X}_p$, respectively. Then the material properties and surface tension are evaluated using the predicted front position as

$$\rho^{n+1} = \rho(\widetilde{\mathbf{X}}_p^{n+1}); \quad \mu^{n+1} = \mu(\widetilde{\mathbf{X}}_p^{n+1}); \quad \mathbf{f}_b^{n+1} = \mathbf{f}_b(\widetilde{\mathbf{X}}_p^{n+1}). \tag{2.35}$$

The velocity and pressure fields at new physical time level $n+1$ are then computed by solving the flow equations (Eq. 2.13) by the FV method for a single physical time step and finally the positions of the front points are corrected as

$$\mathbf{X}_p^{n+1} = \mathbf{X}_p^n + \frac{\Delta t}{2}(\mathbf{V}_p^n + \mathbf{V}_p^{n+1}). \tag{2.36}$$

After this step the material properties and the body forces are re-evaluated using the corrected front position. The method is second order accurate both in time and space. All terms except $\mathbf{f}_b$ in Eq.(2.13) are treated implicitly in physical time so that the physical time is determined solely by the accuracy considerations and stability constraint mainly due to surface tension.

Perfect reflection boundary conditions are used at the solid boundary for the front marker points, i.e., the front marker points crossing the solid boundary due to numerical error are reflected with respect to the inward normal vector back into the computational domain. If the front marker point is close to the boundary as sketched in Fig. 2.4, the front properties are distributed onto curvilinear cells in a conservative manner, i.e., the weights are defined only for the cells within the computational domain (shown by the thick solid line in the sketch) and are normalized to satisfy the consistency conditions given by Eq.(2.27). The grid properties are interpolated onto the front point in a similar manner.

The Lagrangian grid is initially uniform and is kept nearly uniform throughout the computations by deleting small elements and splitting the large elements in the same way as described by Tryggvason et al. [28]. The initial front element size is typically set to $0.75\Delta l$, where Δl is the minimum size of the curvilinear grid cell. During the simulation, in each physical time step, the elements that are smaller than $0.5\Delta l$ are deleted and the elements that are larger than Δl are splited into two parts in order to keep the Lagrangian grid nearly uniform and to prevent the formation of wiggles much smaller than the grid size.

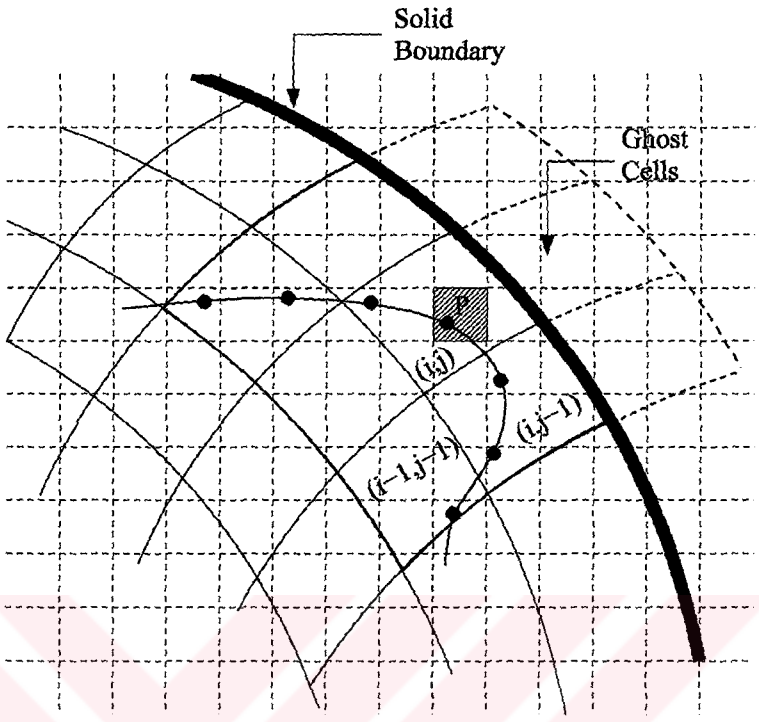

Figure 2.4: Distribution of front properties from the Lagrangian grid onto the curvilinear grid and interpolation of flow quantities from the curvilinear grid onto the Lagrangian grid near a solid boundary.

Chapter 3

RESULTS AND DISCUSSION

The method is first validated for the classical problem of the oscillation of a drop immersed in another fluid. The oscillation is induced by an initial perturbation to the surface configuration of the drop and is damped due to viscous dissipation. The computational results are compared with the analytical solution in terms of the oscillation frequency and damping rate. The method is then applied to compute the motion of a freely falling drop in a straight channel studied earlier by Han and Tryggvason [7] using a finite-difference/front-tracking (FD/FT) method. Finally the method is used to compute the motion of freely rising drops due to buoyancy in a continuously constricted channel studied experimentally by Hemmat and Borhan [8].

3.1 Oscillating Drop

The first test case concerns with the classical problem of an axisymmetric oscillating drop. The oscillation is induced by initial perturbations to the drop surface configuration and is damped due to viscous damping. Consider a drop of liquid with perturbed radius in the form

$$r = a\left(1 + \frac{\zeta}{4}(1 + 3\cos 2\theta)\right), \tag{3.1}$$

where a is the equivalent drop radius, ζ is magnitude of the perturbation and θ is the polar angle measured from the axis of symmetry. Note that this form of deformation conserves the volume of the drop of radius a [5]. When the drop is perturbed, surface tension tries to draw the interface back into a spherical configuration causing the surface to oscillate. Lamb [13] showed that the oscillation frequency is given by

$$\omega_n^2 = \frac{n(n+1)(n-1)(n+2)\sigma}{[(n+1)\rho_d + n\rho_o]a^3}, \tag{3.2}$$

with the period

$$\tau_{th} = \frac{2\pi}{\omega_n}, \tag{3.3}$$

where n is the mode of oscillation with $n = 2$ being the primary mode and σ is the surface tension coefficient. Neglecting the effects of the ambient fluid viscosity, the viscous damping time constant is given by

$$\tau_\nu = \frac{1}{(n-1)(2n+1)} \frac{a^2}{\nu}, \tag{3.4}$$

where ν is the kinematic viscosity of the drop fluid. Figure 3.1 shows the evolution of the

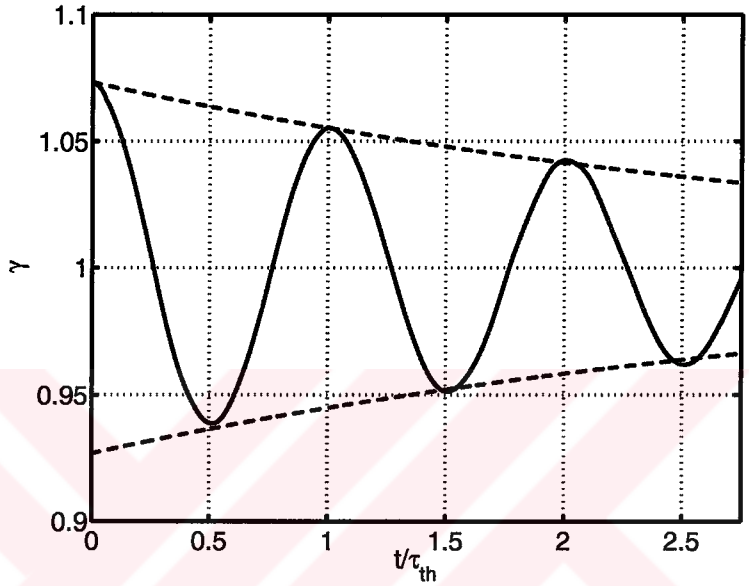

Figure 3.1: The deformation γ versus nondimensional time for an oscillating drop immersed in the host-fluid with the perturbation coefficient $\zeta = 0.05$, $\rho_d/\rho_o = 50$ and $\mu_d/\mu_o = 400$. The theoretical rate of decay is shown by dashed lines below and above the oscillating curve.

deformation parameter γ defined as the ratio of the drop radius in the axial direction to the drop radius in the radial direction. The initial perturbation is set to $\zeta = 0.05$. The computational domain is $6a$ in the radial direction and extends to $12a$ in the axial direction, and is resolved by a 192×384 Cartesian grid stretched in the axial and radial directions to better resolve the flow in the vicinity of the drop. Periodic boundary conditions are used in the axial direction and no-penetration, perfect slip boundary conditions are used in the radial direction. The density and kinematic viscosity of the drop fluid are 50 and 400 times larger than the density and kinematic viscosity of the ambient fluid, respectively. The time is nondimensionalized by the theoretical period for the lowest ($n = 2$) mode. The theoretical damping rate is also plotted in Fig. 3.1. It can be seen in this figure that both

the oscillation frequency and damping rate are predicted well with the present method. For example, the error between the computed and theoretical oscillation frequencies is found to be less than 1% at time $t/\tau_{th} = 2.0$ showing the accuracy of the present method for this standard test case.

3.2 Buoyancy-Driven Falling Drop in a Straight Channel

The second test case concerns with buoyancy-driven falling drops in a straight channel studied earlier by Han and Tryggvason [7]. The physical problem and computational domain are sketched in Fig. 3.2. As can be seen in this figure, the ambient fluid completely fills the rigid cylinder and the drop that is denser than the ambient fluid accelerates downward due to gravitational body force. The problem is governed by four nondimensional parameters [7], namely the Eötvös number Eo (interchangeably called the Bond number, Bo), the Ohnesorge number Oh_d, the density and viscosity ratios defined as

$$\begin{aligned} E_o &= \frac{g_z \Delta\rho d^2}{\sigma}, \\ Oh_d &= \frac{\mu_d}{\sqrt{\rho_d d\sigma}}, \\ \rho^* &= \frac{\rho_d}{\rho_o}, \\ \mu^* &= \frac{\mu_d}{\mu_o}, \end{aligned} \tag{3.5}$$

where $\Delta\rho = \rho_d - \rho_o$ is the density difference between the drop and the ambient fluids, g_z is gravitational acceleration and d is the initial drop diameter. The Ohnesorge number based on the ambient fluid is defined similarly as $Oh_o = \frac{\mu_o}{\sqrt{\rho_o d\sigma}}$. The subscripts d and o denote the properties of the drop and ambient fluids, respectively. The nondimensional time is defined as

$$t^* = \frac{t}{\sqrt{d/g_z}}. \tag{3.6}$$

In all the computations presented in this section, the computational domain is $5d$ in radial direction and is $15d$ in the axial direction. No-slip boundary conditions are applied on the cylinder walls and axisymmetry conditions are applied on the centerline. The drop centroid is initially located at $(r_c, z_c) = (0, 12d)$. The computational domain is resolved by a 128×768 regular Cartesian grid. The grid is stretched in the radial direction to have more grid points close to the centerline. The Ohnesorge number, the density and viscosity ratios are kept

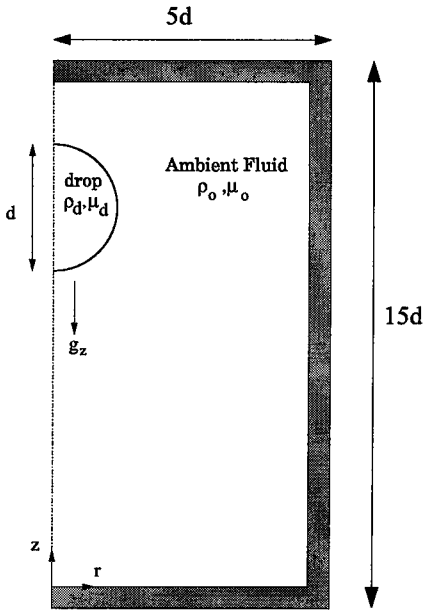

Figure 3.2: Schematic illustration of the physical problem and computational domain for a buoyancy-driven falling drop in a straight channel.

constant at $Oh_d = 0.0466$ ($Oh_o = 0.05$), $\rho_d/\rho_o = 1.15$ and $\mu_d/\mu_o = 1$ in all the results presented here. In Fig. 3.3, the evolution of the drop for $Eo = 12$ and $Eo = 24$ is presented together with the results obtained with the finite-difference/front-tracking (FD/FT) method [7]. As can be seen in this figure, the present results are in a very good qualitative agreement with the results obtained with FD/FT method. To quantify the accuracy of the present method, the velocity is nondimensionalized by $\sqrt{g_z d}$ and the nondimensional velocity of the drop centroid V_c is plotted in Fig. 3.4a together with the FD/FT results. It is clearly seen in this figure that the present results are also in a very good quantitative agreement with those of the FD/FT method demonstrating the accuracy of the present method. Finally the percentage change in drop volume is plotted in Fig. 3.4b as function of nondimensional time both for $Eo = 12$ and $Eo = 24$ cases and are again compared with the results of the FD/FT method. This figure shows that the volume changes in the present and FD/FT methods are of the same order and the maximum volume change at the end of the simulation is smaller than 2.5% in the present method. The relatively large volume change in the present method compared to the FD/FT method may be attributed to the larger numerical error in the

present results partly due to larger physical time steps and partly due to the interpolation and distribution algorithms.

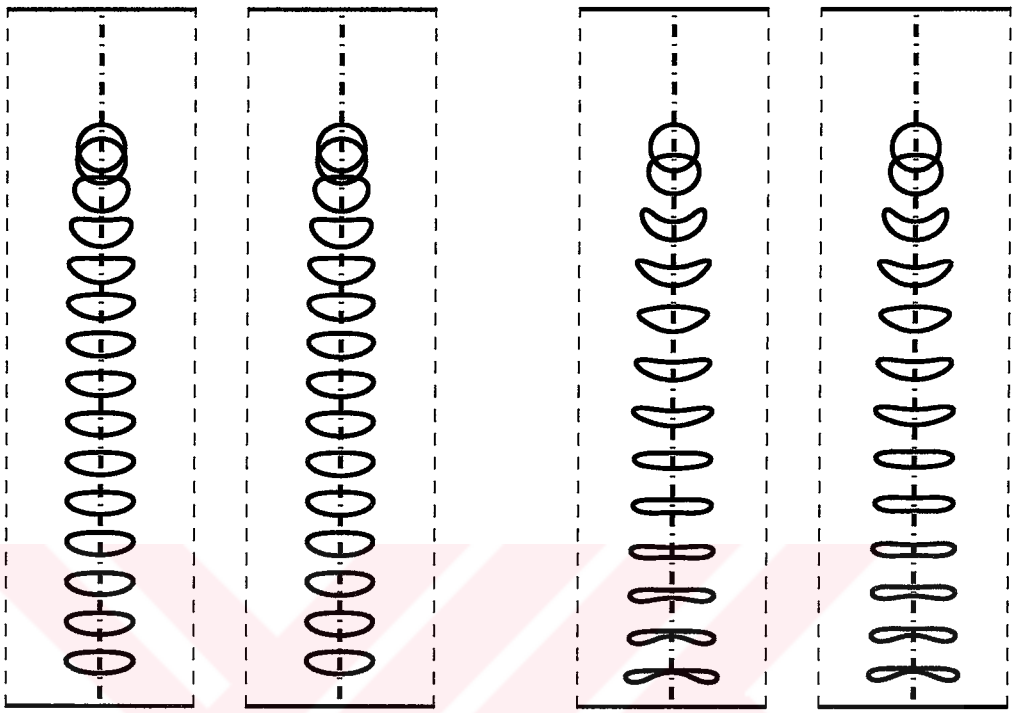

Figure 3.3: Evolution of drop for $Eo = 12$ (left plots) and $Eo = 24$ (right plots). The present results are plotted on the left in each group and the results obtained with the finite-difference/front-tracking (FD/FT) method [7] are plotted on the right. The gap between two successive drops in each column represents the distance the drop travels at a fixed time interval and the last interface is plotted at $t^* = 39.6$ and $t^* = 44.01$ for $Eo = 12$ and $Eo = 24$ cases, respectively.

3.3 Buoyancy-Driven Rising Drops in a Continuously Constricted Channel

The previous two test cases have confirmed the accuracy of the present method. The final test case concerns with the buoyancy-driven motion of viscous drops through a vertical capillary with periodic corrugations studied experimentally by Hemmat and Borhan [8]. The computational setup is sketched in Fig. 3.5a. The capillary tube consists of a 26 cm

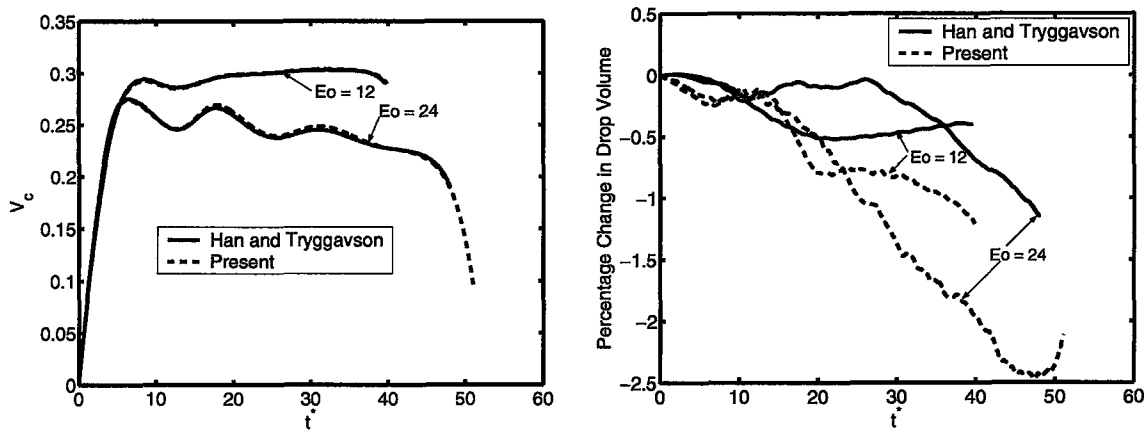

Figure 3.4: (a) Centroid velocity (b) percentage change in drop volume versus t^* for $Eo = 12$ and $Eo = 24$ cases. The dashed lines are the present results and solid lines are the FD/FT results.

long, periodically constricted cylindrical tube with 6 corrugations. The average internal radius of the tube is $R = 0.5$ cm, and the wavelength and amplitude of the corrugations are $h = 4$ cm and $A = 0.07$ cm, respectively. The suspending fluids are an aqueous glycerol solution (denoted by GW3) and diethylene glycol-glycerol mixtures (denoted by DEGG10 and DEGG12). A variety of UCON oils are used as drop fluids. The properties of the drop and suspending fluids are summarized in Table 3.1 where the same label is used for each system as that used by Hemmat and Borhan [8]. A complete description of the experimental set up can be found in [8]. A portion of a coarse grid containing 8×416 grid cells is plotted in Fig. 3.5b to show the overall structure of the body-fitted grid used in the simulations. The average rise velocity of buoyant drops as well as the drop shapes are computed and the results are compared with the experimental data [8] for a range of the governing parameters, viz. the dimensionless drop size, κ, defined as the ratio of the equivalent spherical drop radius to the average capillary radius, the ratio of the drop to the suspending fluid viscosities, λ, the corresponding ratio of fluid densities γ, and the Bond number $Bo = \Delta\rho g_z R^2/\sigma$, representing the ratio of buoyancy to interfacial tension forces; $\Delta\rho$ and σ denote the density difference and interfacial tension between the drop and suspending fluid, respectively, and g_z is the gravitational acceleration.

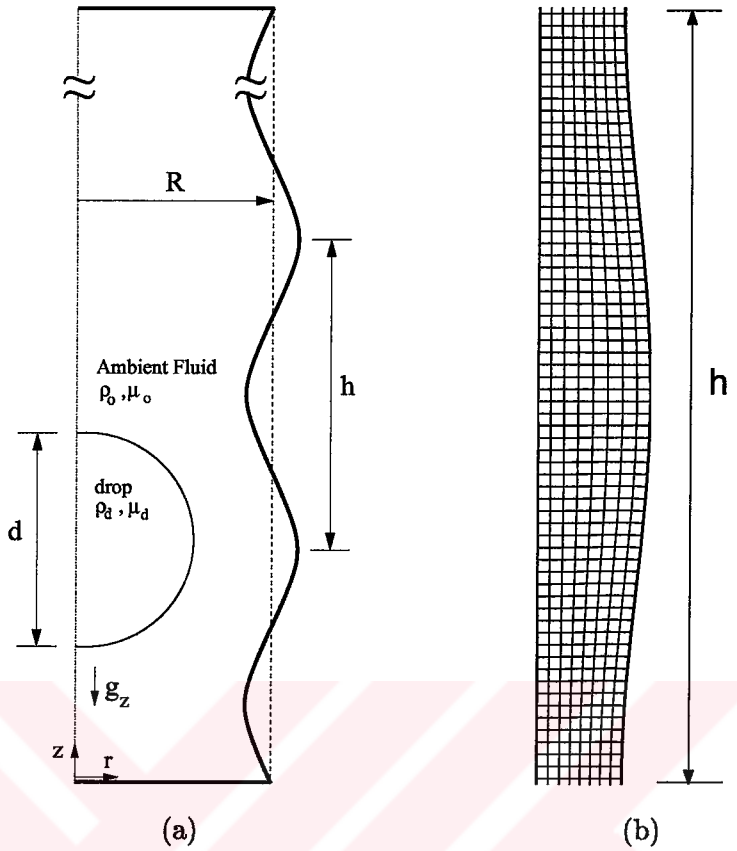

Figure 3.5: (a) Schematic illustration of the computational setup for a buoyancy-driven rising drop in a constricted channel. (b) A portion of a coarse computational grid containing 8×416 cells.

In all the results presented in this section, the drops are initially located at $z = 1.5h$ in the ambient fluid that fully fills the cylindrical tube and is initially in the hydrostatic conditions. Symmetry boundary conditions are applied along the centerline and no-slip boundary conditions are used at top, bottom and lateral surfaces of the cylindrical tube. Drops are initially stationary and start rising due to buoyancy. The drops are initially spherical if the initial drop radius is smaller than the capillary tube and are ellipsoidal otherwise. Note that d represents the equivalent drop diameter if the initial shape of the drop is not spherical. We consider three systems labeled as GW3, DEGG10 and DEGG12 (Table 3.1). It is emphasized here that, in addition to the reported measurement error up to 5% in the experimental data, there is inconsistency between the material properties and the non-dimensional numbers especially for system DEGG12.

System	Suspending fluid	Drop fluid	μ_o (mPa·s)	μ_d (mPa·s)	ρ_o (kg/m^3)	ρ_d (kg/m^3)	σ (N/m)
GW3	glycerol-water (96.2wt%)	UCON-1145	450	530	1250	995	0.0105
DEGG10	diethylene-glycol (100.0wt%)	UCON-165	28	63	1110	975	0.0016
DEGG12	diethylene glycol-glycerol (63.8wt%)	UCON-285	87	115	1160	966	0.0042

Table 3.1: Two-phase systems used in the computations

For instance, the Bond number reported by Hemmat and Borhan [8] is about 10% larger than the value we computed directly from the given material properties and the average tube radius.

The results are expressed in terms of non-dimensional quantities denoted by superscript "*". The dimensionless coordinates are defined as $z^* = z/h$ and $r^* = r/R$. Time and velocity are made dimensionless with $T_{\text{ref}} = \frac{\mu_o}{\Delta\rho g_z R}$ and $V_{\text{ref}} = \frac{\Delta\rho g_z R^2}{\mu_o}$, respectively.

First a qualitative analysis of the shapes of the drops are shown in Fig. 3.6. In this figure, a sequence of images for the evolution of the shapes of viscous drops through constricted channel are plotted for GW3 and DEGG12 systems with the nondimensional drop sizes $\kappa = 0.54$, 0.78 and 0.92. The computations are performed on a 32×1664 grid, the physical time step is $\Delta t^* = 1.641$ and the residuals are reduced by three orders of magnitude in each sub-iteration. As can be seen in these figures, when a large drop ($\kappa > 0.7$) reaches a constriction, its leading edge follows the capillary wall contour and squeezes through the throat. Once the leading meniscus clears the throat, its rise velocity increases as it enters the diverging cross-section while the trailing edge of the drop remains trapped behind the throat similar to the experimental observations [8].

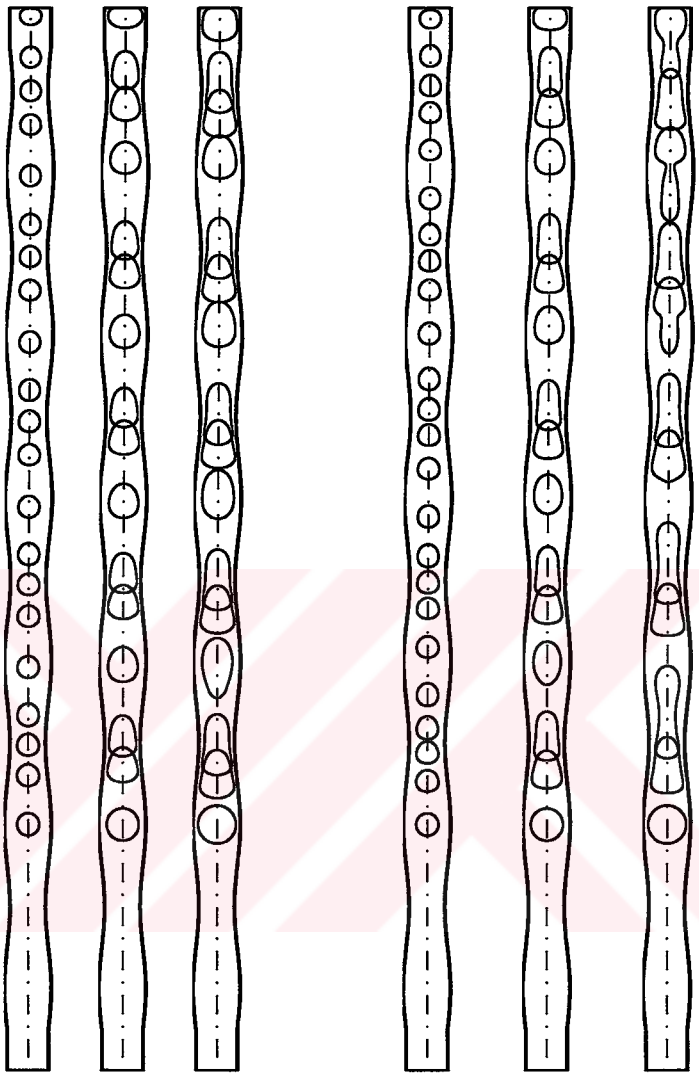

Figure 3.6: Snapshots of buoyant drops of GW3 system (a) and DEGG12 system (b) for drops sizes $\kappa = 0.54$, 0.78 and 0.92 from left to right for each system. The gap between two successive drops in each column represents the distance the drop travels at a fixed time interval and the last interface is plotted from left to right at $t^* =$ (a) 1044.4, 783.3, 783.3 and (b) 2831.3, 3693.0 and 5416.4, respectively.

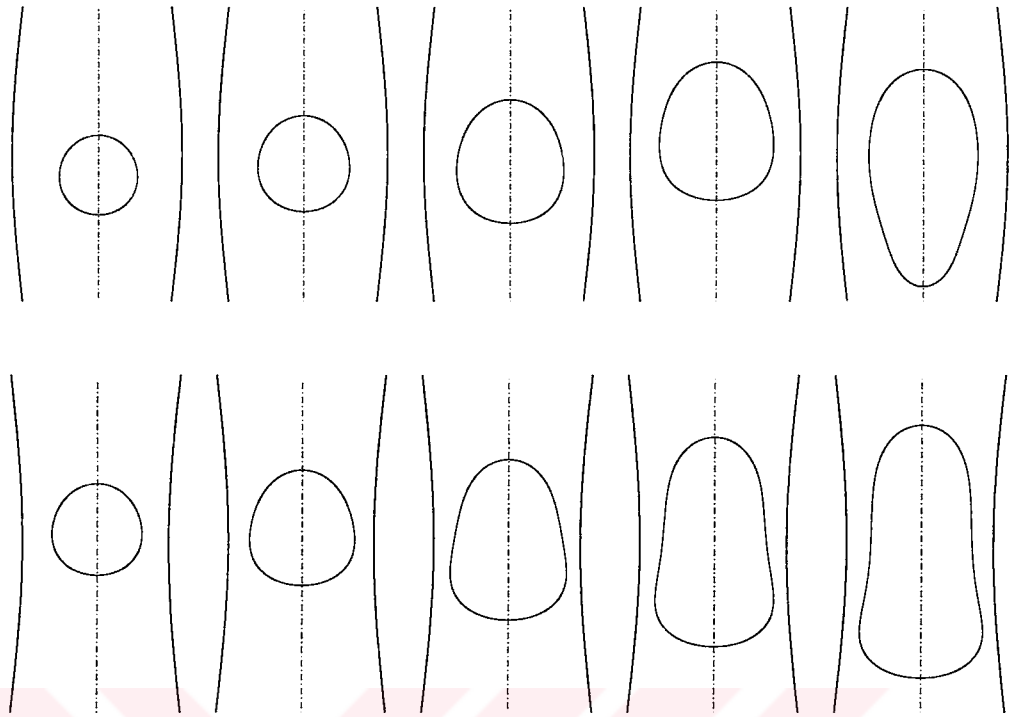

Figure 3.7: Snapshots of the drops at the expansion (upper plots) and at the throat (lower plots) of the constriction for the GW3 system for drop sizes (from left to right) $\kappa = 0.54,\ 0.65,\ 0.78,\ 0.85$ and 0.92, respectively. Grid: 32×1664, $\Delta t^* = 0.418$.

To better show the effects of the constrictions, the snapshots of the drops before and after the throat of the constriction are shown in Figs. 3.7 and 3.8 for GW3 and DEGG12 systems, respectively, for drop sizes $\kappa = 0.54,\ 0.65,\ 0.78,\ 0.85$ and 0.92. As can be seen in these figures, the drop shapes are smooth in all the cases indicating accuracy of the computations. Note that these drop shapes qualitatively compare well with the experimental observations published by Hemmat and Borhan [8]. The drop shapes, the velocity field and pressure contours in the vicinity of the drop are plotted in Fig. 3.9 for a DEGG12 drop with $\kappa = 0.92$ while it passes through the throat and just after the throat to better show the overall quality of the solution. Finally the vertical drop tip location scaled by the corrugation wavelength and the drop tip rise velocity scaled by the reference velocity V_{ref} are plotted against the non-dimensional time in Figs. 3.10 and 3.11 for GW3 and DEGG12 systems, respectively, for various drop sizes.

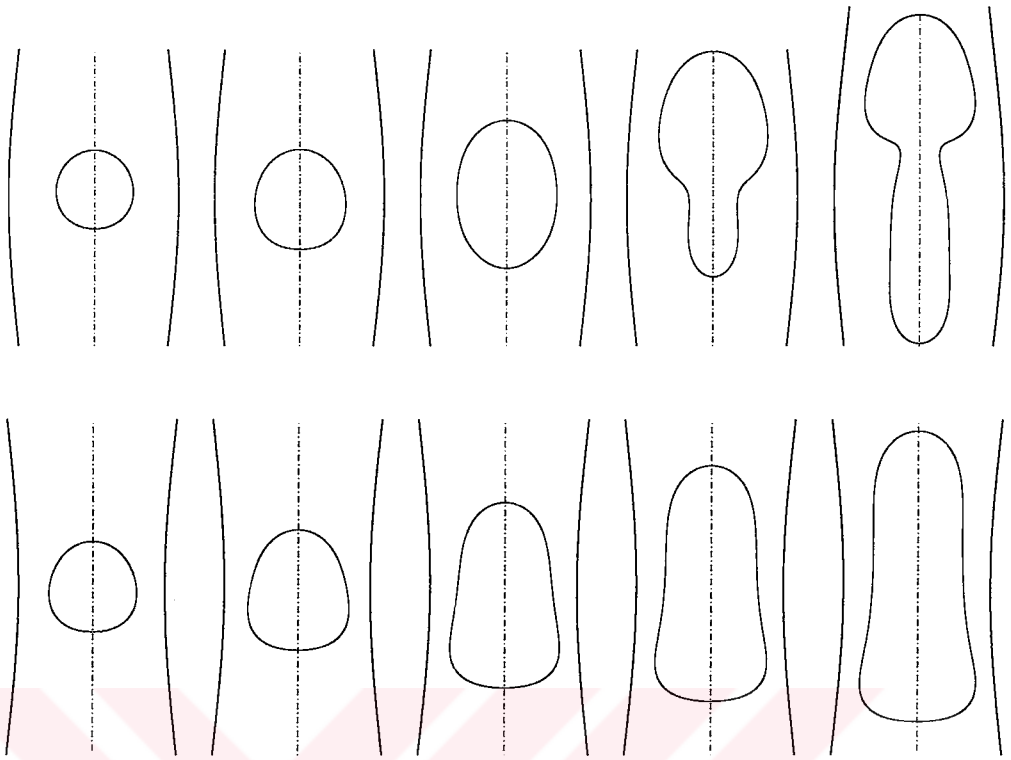

Figure 3.8: Snapshots of the drops at the expansion (upper plots) and at the throat (lower plots) of the constriction for the DEGG12 system for drop sizes (from left to right) $\kappa =$ 0.54, 0.65, 0.78, 0.85 and 0.92, respectively. Grid: 32×1664, $\Delta t^* = 1.641$.

The retardation effect of the constrictions is clearly seen in these figures for large drops, i.e., $\kappa > 0.7$. It is also seen that the drops quickly accelerate and reach a periodic motion in all the cases.

3.4 Numerical Accuracy and Convergence

The numerical accuracy and convergence of the method are examined in this section. The numerical error can be decomposed into spatial and time-stepping errors. The spatial error results from the spatial discretization in the FV method and the interpolation and distribution schemes used in the front-tracking method due to finite size of mesh cells. The leading spatial error is expected to be second order accurate. The grid convergence is demonstrated here only for a DEGG12 drop of size $\kappa = 0.92$ but similar results are observed for the other systems.

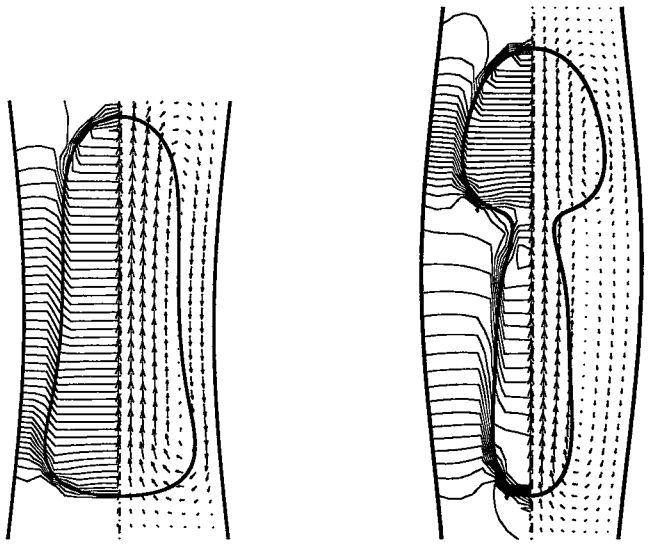

(a) (b)

Figure 3.9: Velocity vectors (right portion) and pressure contours (left portion) in the vicinity of the DEGG12 drop with $\kappa = 0.92$ while it passes through (a) the throat and (b) the expansion regions. Grid: 32×1664, $\Delta t^* = 1.641$.

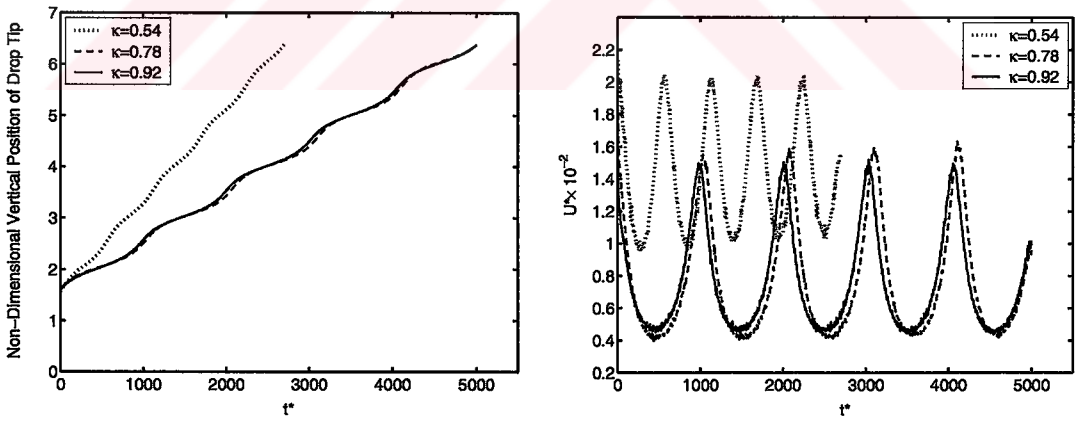

(a) (b)

Figure 3.10: The non-dimensional vertical positions (left plot) and the non-dimensional rise velocities (right plot) of the drop tip plotted against the non-dimensional time t^* for the drops of GW3 system with $\kappa = 0.54, 0.78$ and 0.92. Grid: 32×1664, $\Delta t^* = 0.418$.

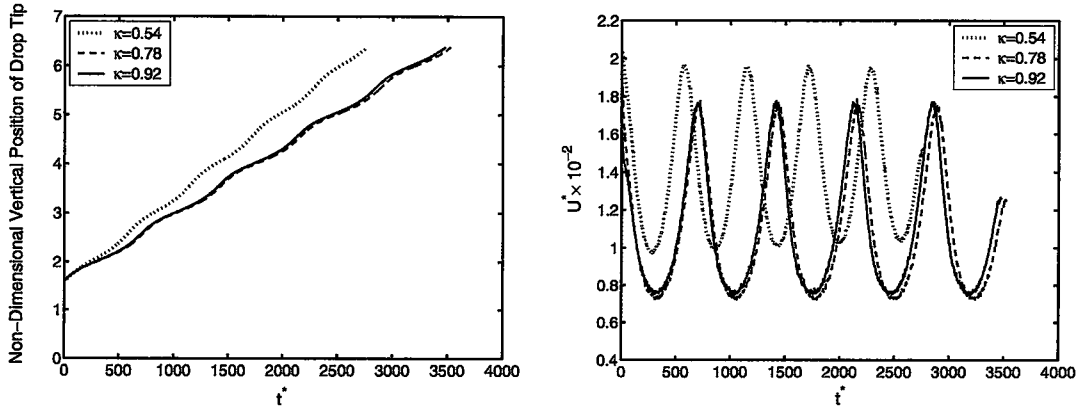

Figure 3.11: The non-dimensional vertical positions (left plot) and the non-dimensional rise velocities (right plot) of the drop tip plotted against the non-dimensional time t^* for the drops of DEGG12 system with $\kappa = 0.54, 0.78$ and 0.92. Grid: 32×1664, $\Delta t^* = 1.641$.

The non-dimensional rise velocity of the drop centroid versus the non-dimensional axial length is plotted in Fig. 3.12 to show the overall dependence of the calculated results on grid refinement. The physical time step is taken as $\Delta t^* = 1.641$ and the residuals are reduced by three orders of magnitude in each inner iteration. The dashed vertical lines shown in Fig. 3.12 are drawn to mark the locations (Table 3.2) where the spatial error is quantified as will be discussed below. As can be seen in this figure, the difference among the results is decreasing with grid refinement, indicating that grid convergence is achieved and 32×1664 grid is sufficient for this case. To quantify the spatial error and to verify the expected second-order spatial accuracy, the rise velocity of the drop centroid is plotted against the inverse of the total number of grid cells M^{-2} in Fig. 3.13. The symbols indicate the numerical results and the lines are the linear least-squares fits to the numerical data. The approximate linear relationship between the rise velocity of drop centroid and M^{-2} in the asymptotic range confirms the expected second order accuracy of the method in space. To show the time-stepping error convergence, the non-dimensional rise velocity of the drop centroid is plotted against the non-dimensional time in Fig. 3.14 for various time steps.

	Axial Distance(z^*)
Location 1	2.35
Location 2	2.70
Location 3	3.27
Location 4	3.50

Table 3.2: Four selected locations used to quantify the spatial error.

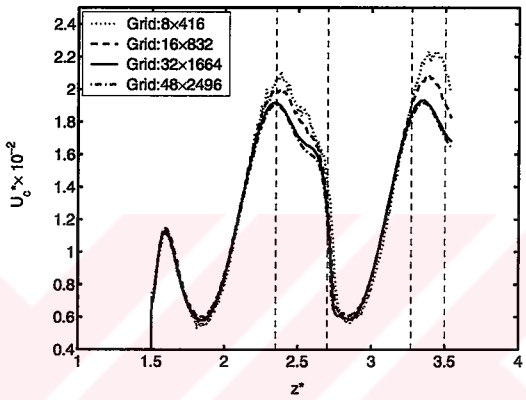

Figure 3.12: The non-dimensional centroid velocity of a DEGG12 drop with $\kappa = 0.92$ plotted against the non-dimensional axial distance computed on 8×416, 16×832, 32×1664, and 48×2496 grids. $\Delta t^* = 1.641$.

The computations are performed on a 32×1664 grid and the residuals are reduced by three orders of magnitude. As can be seen in this figure, the small difference between results obtained with different time steps indicates small time-stepping error in the present method. Note that larger time steps are found to result in instabilities on drop surface mainly due to explicit treatment of surface tension. The vertical dashed lines are again drawn to mark the locations (Table 3.3) where the time-stepping error is quantified. Figure 3.15 shows the rise velocity of the drop centroid against Δt^2. The symbols are the numerical results and the solid lines are the linear least-squares fits to the numerical data. This figure shows that the slopes of the linear least-squares fits are small indicating the small time-stepping error in the simulations. Finally the effects of the error tolerance are analyzed to determine the required

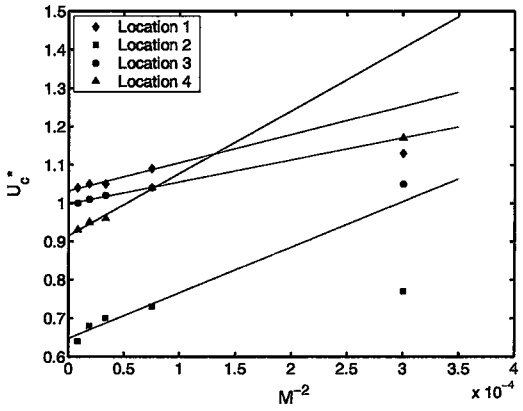

Figure 3.13: The non-dimensional centroid velocities of a DEGG12 drop with $\kappa = 0.92$ against the inverse of the total number of grid cells M^{-2} at the selected locations (Table 3.2) showing the expected second order accuracy of the method. The solid lines are linear least-square fits to the numerical data. $\Delta t^* = 1.641$.

	Time(t^*)
Time 1	901
Time 2	999
Time 3	1350
Time 4	1459

Table 3.3: Four selected physical times used to quantify the time-stepping error.

reduction in averaged residuals in FV inner iterations. The error tolerance is denoted by ϵ_{res} and is defined as the reduction in average residuals in FV inner iterations. Figure 3.16 shows the non-dimensional velocity of the drop centroid plotted against the non-dimensional time for various error tolerances. It is clearly seen in this figure that $\epsilon_{res} = 10^{-3}$ is sufficient for this test case. Although not shown here, $\epsilon_{res} = 5 \times 10^{-3}$ is also found to be sufficient but $\epsilon_{res} = 10^{-3}$ is used in all the computations presented in this study.

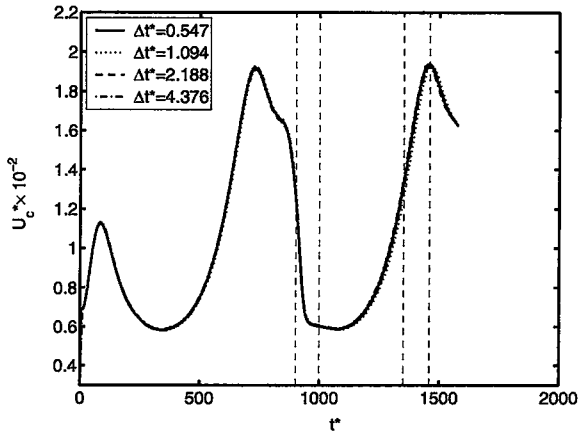

Figure 3.14: The non-dimensional centroid velocity of a DEGG12 drop with $\kappa = 0.92$ plotted against the non-dimensional time computed with $\Delta t^* = 0.547$, 1.094, 2.188, and 4.376. *Grid* : 32 × 1664.

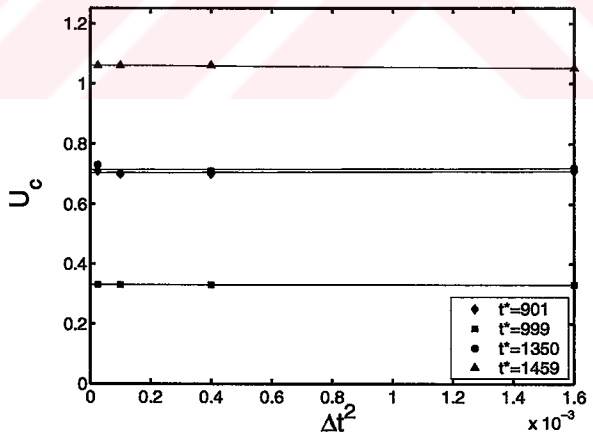

Figure 3.15: The centroid velocities of a DEGG12 drop with $\kappa = 0.92$ against the time step Δt at the selected time frames (Table 3.3). The solid lines are linear least-square fits to the numerical data. *Grid* : 32 × 1664.

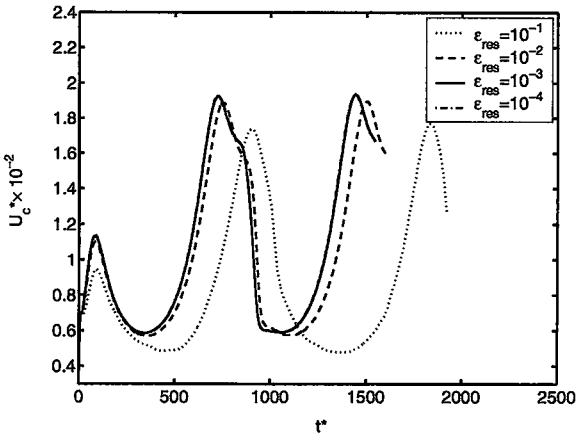

Figure 3.16: The non-dimensional centroid velocity of a DEGG 12 drop with $\kappa = 0.92$ against the non-dimensional time computed with the inner iteration error tolerances of $\epsilon_{\text{res}} = 10^{-1}$, 10^{-2}, 10^{-3} and 10^{-4}. *Grid* : 32×1664 and $\Delta t^* = 1.641$.

3.5 Comparison with the Experimental Data

To demonstrate the performance of the present FV/FT method, the numerical results are compared with the experimental data [8]. All the results are obtained on a 32×1664 grid, the physical time step is set to $\Delta t^* = 1.641$ and the error tolerance for sub-iterations is fixed at $\epsilon_{res} = 10^{-3}$. In order to qualitatively characterize the evolving shapes of drops as they pass through the corrugations, a deformation parameter denoted by D is defined as the ratio of the perimeter of the deformed drop profile to that of the equivalent spherical drop. The variations of the deformation parameter as a function of the axial position of the drop within one period of corrugation are plotted in Figs. 3.17a and 3.17b for GW3 and DEGG12 systems, respectively, and are compared with the experimental data. It can be seen in these figures that the general trend for the deformation parameter is well captured by the present computations for both GW3 and DEGG12 systems. The deformation is negligibly small for small drops, i.e., drops with $\kappa < 0.60$, and increases rapidly as the drop size gets larger. The axial length of drop profile scaled by the wavelength of corrugation is denoted by L and is plotted in Figs. 3.18a and 3.18b for GW3 and DEGG12 systems, respectively.

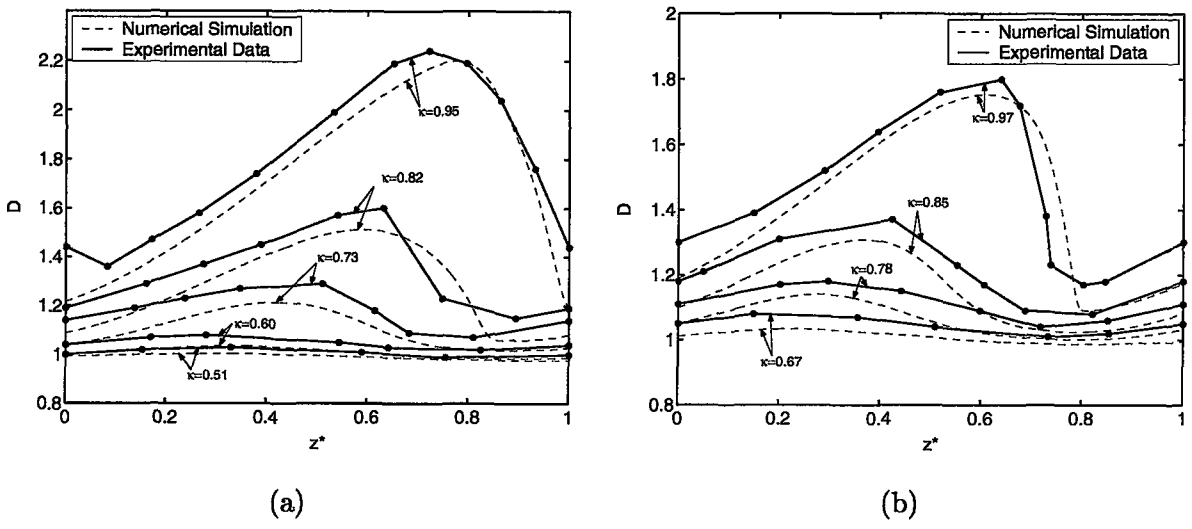

Figure 3.17: The variations of the deformation parameter D with axial position of the advancing meniscus within one period of corrugation for (a) DEGG12 system and (b) GW3 system. The dashed curves are the numerical results and the solid lines are the experimental data [8].

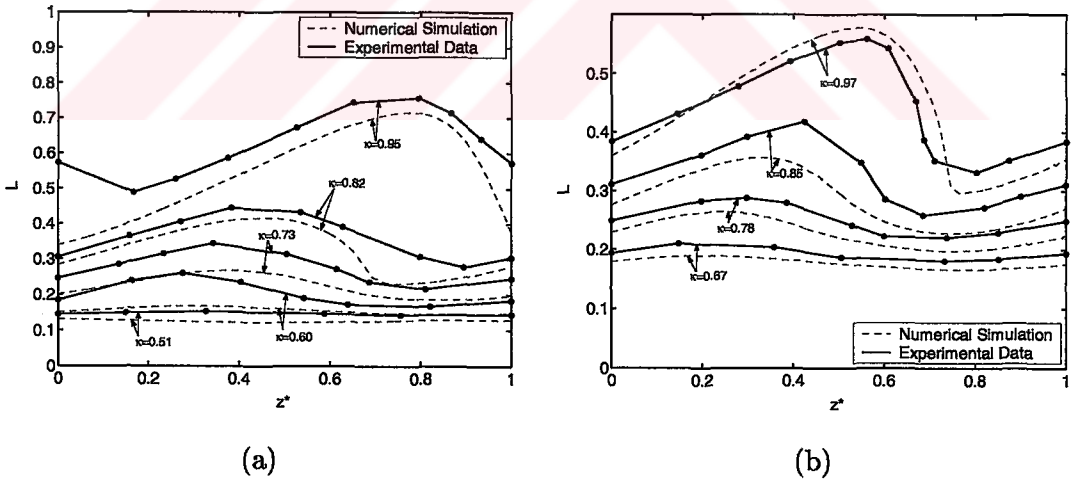

Figure 3.18: The variations of the drop length L with axial position of the advancing meniscus within one period of corrugation for (a) DEGG12 system and (b) GW3 system. The dashed curves are the numerical results and the solid lines are the experimental data [8].

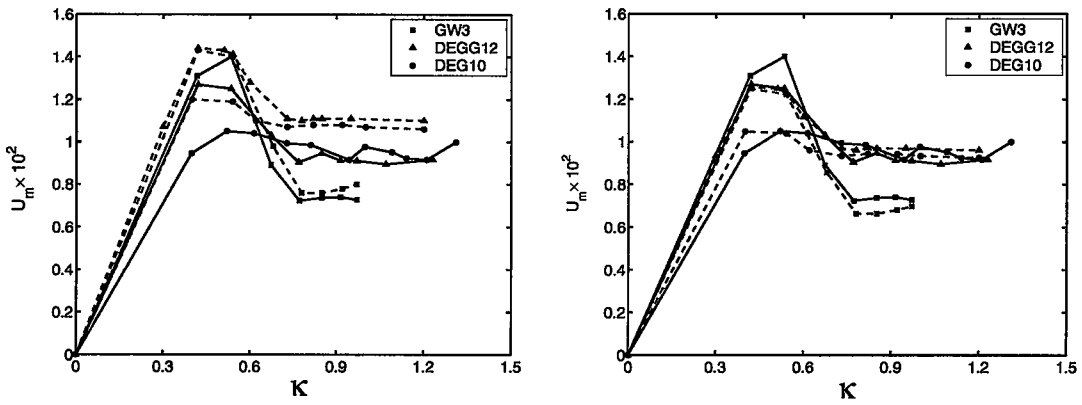

Figure 3.19: Dimensionless average rise velocity as a function of drop size. The dashed curves are the numerical results and the solid lines are the experimental data. The numerical results are obtained with (a) the average tube radius of $R = 0.5$ cm and (b) the modified tube radius of $R = 0.535$ cm that yields the same Bond number given by Hemmat and Borhan [8].

The numerical results for L are compared with the experimental data for various drop sizes. It is clear from these figures that the general trend for L is also well captured by the present computations. The discrepancy between the computed and the experimental results for D and L are partly attributed to the uncertainties in the experimental data and the inconsistency between the Bond number reported by Hemmat and Borhan [8] and the Bond number computed from the material properties and the average tube radius.

Finally the computed average rise velocities are compared with the experimental data. The non-dimensional average rise velocity U_m is plotted against the non-dimensional drop size κ in Fig. 3.19a for GW3, DEGG10 and DEGG12 systems. The average rise velocity is defined as the average velocity of the drop centroid in the periodic motion. As can be seen in this figure, the numerical results are in a good agreement with the experimental data, i.e., the trend is well captured and the maximum error is less than 10% for all the cases.

In addition, if the inconsistency between the Bond numbers mentioned above is taken into account by modifying the average tube radius to match the given Bond number in [8], the computed results match much better with the experimental data as shown in Fig. 3.19b. In this case, the difference between the computed and experimental data reduces below a few percent. In Fig. 3.19, the retardation effect of the constrictions is clearly seen and the non-dimensional velocity remains essentially constant for large drops, i.e., $\kappa > 0.90$ for all the cases.

Chapter 4

CONCLUSIONS

A finite-volume/front-tracking (FV/FT) method has been developed for computations of dispersed multiphase flows in complex geometries. The method is based on the one-field formulation of the flow equations and treating the different phases as a single fluid with variable material properties. The flow equations are solved by a FV method on a body-fitted curvilinear grid and a separate Lagrangian grid is used to represent the interfaces between different phases. A novel tracking algorithm that utilizes an auxiliary uniform Cartesian grid is developed to track the interfaces on the curvilinear grid and is found to be robust and computationally efficient. The front-tracking methodology is extended to body-fitted curvilinear grids and is combined with a newly developed finite-volume method to facilitate accurate and efficient modeling of strong interactions between the phases and complex solid boundary.

The FV method is based on the concept of dual-time stepping with added fourth order dissipation and time integration is done by a block diagonal alternating direction implicit (ADI) scheme. Several convergence acceleration techniques such as preconditioning, local time-stepping and multigrid methods are used to accelerate the convergence of the sub-iterations in the FV algorithm. The spatial derivatives are approximated using central differences and fourth order numerical dissipation terms are added to stabilize the scheme.

The method is implemented to solve two-dimensional (plane or axisymmetric) dispersed multiphase flows and has been successfully applied to several test cases including the classical problem of a vibrating drop, buoyancy-driven falling drops in a straight channel and buoyancy-driven rising drops in a continuously constricted channel. It is demonstrated that the method is convergent in terms of grid refinement, time-stepping error and residual reduction in the inner iteration of the FV method. The method is first validated for the classical problem of the oscillation of a drop immersed in another fluid. The computational results are compared with the analytical solution in terms of the oscillation frequency and

damping rate. The error between the computed and theoretical oscillation frequencies is found to be less than 1% showing the accuracy of the present method for this standard test case. The second test case is used to compare the performance of the present method with that of the FD-FT method [28, 32]. The method is applied to compute the motion of a freely falling drop in a straight channel and the present results are in a very good quantitative and qualitative agreement with those of the FD/FT method demonstrating the accuracy of the present method. The relatively large volume change of the drop in the present method compared to the FD/FT method may be attributed to the larger numerical error in the present results partly due to larger physical time steps and partly due to the interpolation and distribution algorithms.

The first two test cases have confirmed the accuracy of the present method. The final test case concerns with the buoyancy-driven motion of viscous drops through a vertical capillary with periodic corrugations studied experimentally by Hemmat and Borhan [8]. In order to qualitatively verify the performance of the present method, the evolving shapes of drops as they pass through the corrugations are compared and the shapes are found to match very well with the experimental results of Hemmat and Borhan [8]. The general trend for the deformation and the length parameter is also well captured by the present computations for both GW3 and DEGG12 systems. The discrepancy between the computed and the experimental results for D and L are partly attributed to the uncertainties in the experimental data and the inconsistency between the Bond number reported by Hemmat and Borhan [8] and the Bond number computed from the material properties and the average tube radius. Hence, based on the present results and the results obtained form [12] it is found that the present method is a viable tool for accurate modeling of dispersed multiphase flows in complex geometries.

Future work includes simulating freely rising air bubbles in constricted capillaries studied experimentally by Hemmat and Borhan[8], as well as the cases where break-up of drops takes place. Simulations of biofluid dynamics is also possible if further improvement of the FV-FT method is achieved under very low Reynolds numbers. The method can be then applied to simulations of white and red blood cells through bifurcating capillaries in the circulation system. In particular, adhesion dynamics of leukocytes to ligand-coated surfaces can be modeled and simulated within the framework of finite-volume/front-tracking methodology.

Appendix A

MATHEMATICAL FORMULATION

The incompressible Navier-Stokes equations for a two-dimensional (plane/axisymmetric) flow can be written in cylindrical coordinates in vector form as [11]

$$\frac{\partial \bar{\mathbf{q}}}{\partial t} + \frac{\partial \bar{\mathbf{f}}}{\partial r} + \frac{\partial \bar{\mathbf{g}}}{\partial z} + \alpha \bar{\mathbf{h}} = \frac{\partial \bar{\mathbf{f}}_v}{\partial r} + \frac{\partial \bar{\mathbf{g}}_v}{\partial z} + \alpha \bar{\mathbf{h}}_v + \bar{\mathbf{f}}_b, \tag{A.1}$$

where

$$\bar{\mathbf{q}} = \begin{Bmatrix} 0 \\ \rho v_r \\ \rho v_z \end{Bmatrix}, \quad \bar{\mathbf{f}} = \begin{Bmatrix} v_r \\ \rho v_r^2 + p \\ \rho v_r v_z \end{Bmatrix}, \quad \bar{\mathbf{g}} = \begin{Bmatrix} v_z \\ \rho v_r v_z \\ \rho v_z^2 + p \end{Bmatrix}, \quad \bar{\mathbf{h}} = \frac{1}{r} \begin{Bmatrix} v_r \\ \rho v_r^2 \\ \rho v_r v_z \end{Bmatrix}, \tag{A.2}$$

and

$$\bar{\mathbf{f}}_v = \begin{Bmatrix} 0 \\ \bar{\tau}_{rrp} \\ \bar{\tau}_{zr} \end{Bmatrix}, \quad \bar{\mathbf{g}}_v = \begin{Bmatrix} 0 \\ \bar{\tau}_{zr} \\ \bar{\tau}_{zzp} \end{Bmatrix}, \quad \bar{\mathbf{h}}_v = \begin{Bmatrix} 0 \\ \bar{\tau}_{rrp} - \bar{\tau}_{\theta\theta} - \frac{2}{3}\mu\frac{v_r}{r} - \frac{2}{3}r\frac{\partial}{\partial r}(\mu\frac{v_r}{r}) \\ \bar{\tau}_{zr} - \frac{2}{3}r\frac{\partial}{\partial z}(\mu\frac{v_r}{r}) \end{Bmatrix}. \tag{A.3}$$

The viscous stresses appearing in the viscous flux vectors are given by

$$\begin{aligned}
\bar{\tau}_{zzp} &= \frac{4}{3}\mu\frac{\partial v_z}{\partial z} - \frac{2}{3}\mu\frac{\partial v_r}{\partial r}, \\
\bar{\tau}_{zz} &= \bar{\tau}_{zzp} - \frac{2}{3}\mu\frac{v_r}{r} = \frac{4}{3}\mu\frac{\partial v_z}{\partial z} - \frac{2}{3}\mu\left(\frac{\partial v_r}{\partial r} + \frac{v_r}{r}\right), \\
\bar{\tau}_{rrp} &= \frac{4}{3}\mu\frac{\partial v_r}{\partial r} - \frac{2}{3}\mu\frac{\partial v_z}{\partial z}, \\
\bar{\tau}_{rr} &= \bar{\tau}_{rrp} - \frac{2}{3}\mu\frac{v_r}{r} = \frac{4}{3}\mu\frac{\partial v_r}{\partial r} - \frac{2}{3}\mu\left(\frac{\partial v_z}{\partial z} + \frac{v_r}{r}\right), \\
\bar{\tau}_{zr} &= \mu\left(\frac{\partial v_z}{\partial r} + \frac{\partial v_r}{\partial z}\right), \\
\bar{\tau}_{\theta\theta} &= -\frac{2}{3}\mu\left(\frac{\partial v_z}{\partial z} + \frac{\partial v_r}{\partial r}\right) + \frac{4}{3}\mu\frac{v_r}{r}.
\end{aligned} \tag{A.4}$$

In Eq.(A.1) $\alpha = 1$ corresponds to the axisymmetric case and $\alpha = 0$ corresponds to the two dimensional planer case. The continuity equation and linear momentum equations can be

written explicitly as

$$\frac{\partial v_r}{\partial r} + \frac{\partial v_z}{\partial z} + \frac{v_r}{r} = 0, \tag{A.5}$$

$$\frac{\partial \rho v_r}{\partial t} + \frac{\partial(\rho v_r^2 + p)}{\partial r} + \frac{\partial(\rho v_r v_z)}{\partial z} + \frac{1}{r}\rho v_r^2 = \frac{\partial}{\partial r}(\bar{\tau}_{rrp}) + \frac{\partial}{\partial z}(\bar{\tau}_{zr}) + \frac{1}{r}\left(\bar{\tau}_{rrp} - \bar{\tau}_{\theta\theta} - \frac{2}{3}\mu\frac{v_r}{r} - \frac{2}{3}r\frac{\partial}{\partial r}\left(\mu\frac{v_r}{r}\right)\right), \tag{A.6}$$

$$\frac{\partial \rho v_z}{\partial t} + \frac{\partial(\rho v_r v_z)}{\partial r} + \frac{\partial(\rho v_z^2 + p)}{\partial z} + \alpha\frac{\rho v_r v_z}{r} = \frac{\partial}{\partial r}(\bar{\tau}_{zr}) + \frac{\partial}{\partial z}(\bar{\tau}_{zzp}) + \frac{1}{r}\left(\bar{\tau}_{zr} - \frac{2}{3}r\frac{\partial}{\partial z}\left(\mu\frac{v_r}{r}\right)\right). \tag{A.7}$$

Multiplying Eq.(A.5) by r yields

$$\frac{\partial(r v_r)}{\partial r} + \frac{\partial(r v_z)}{\partial z} = 0. \tag{A.8}$$

Similarly, multiplying both sides of Eq.(A.6) by r gives

$$\frac{\partial(\rho r v_r)}{\partial t} + \frac{\partial(\rho r v_r^2 + pr)}{\partial r} + \frac{\partial(\rho r v_r v_z)}{\partial z} - p = (VT)_I, \tag{A.9}$$

where $(VT)_I$ denotes the viscous terms given by

$$(VT)_I = r\left[\frac{\partial}{\partial r}(\bar{\tau}_{rrp}) + \frac{\partial}{\partial z}(\bar{\tau}_{zr}) + \frac{1}{r}\left(\bar{\tau}_{rrp} - \bar{\tau}_{\theta\theta} - \frac{2}{3}\mu\frac{v_r}{r} - \frac{2}{3}r\frac{\partial}{\partial r}\left(\mu\frac{v_r}{r}\right)\right)\right], \tag{A.10}$$

or

$$(VT)_I = \frac{\partial}{\partial r}(r\bar{\tau}_{rrp}) + \frac{\partial}{\partial z}(r\bar{\tau}_{zr}) - \bar{\tau}_{\theta\theta} - \frac{2}{3}\mu\frac{v_r}{r} - \frac{2}{3}r\frac{\partial}{\partial r}\left(\mu\frac{v_r}{r}\right). \tag{A.11}$$

After substituting $\bar{\tau}_{rrp}$, $\bar{\tau}_{zr}$, $\bar{\tau}_{\theta\theta}$ into above expression, one obtains

$$(VT)_I = \frac{\partial}{\partial r}\left[r\left(\frac{4}{3}\mu\frac{\partial v_r}{\partial r} - \frac{2}{3}\mu\frac{\partial v_z}{\partial z} + \frac{2}{3}\mu\frac{\partial v_r}{\partial r}\right)\right] + \frac{\partial}{\partial z}\left[r\mu\left(\frac{\partial v_z}{\partial r} + \frac{\partial v_r}{\partial z}\right)\right] + \frac{2}{3}\mu\left(\frac{\partial v_z}{\partial z} + \frac{\partial v_r}{\partial r}\right) - \frac{4}{3}\mu\frac{v_r}{r} - \frac{2}{3}\mu\frac{\partial v_r}{\partial r}, \tag{A.12}$$

and using continuity equation, we can write

$$(VT)_I = \frac{\partial}{\partial r}[\tau_{rr}] + \frac{\partial}{\partial z}[\tau_{zr}] - \frac{\partial}{\partial r}(2\mu v_r) - \frac{\partial}{\partial z}(\mu v_z) - 2\mu\frac{v_r}{r}, \tag{A.13}$$

where,

$$\tau_{rr} = 2\mu\frac{\partial r v_r}{\partial r}, \quad \tau_{zz} = 2\mu\frac{\partial r v_z}{\partial z}, \quad \tau_{zr} = \mu\left(\frac{\partial r v_r}{\partial z} + \frac{\partial r v_z}{\partial r}\right). \tag{A.14}$$

Similarly, multiply Eq.(A.7) by r to obtain

$$\frac{\partial(\rho r v_z)}{\partial t} + \frac{\partial(\rho r v_r v_z)}{\partial r} + \frac{\partial(\rho r v_z^2 + pr)}{\partial z} = (VT)_{II}, \tag{A.15}$$

where

$$(VT)_{II} = \frac{\partial}{\partial r}(\tau_{zr}) + \frac{\partial}{\partial z}(\tau_{zz}) - \frac{\partial}{\partial r}(\mu v_z). \tag{A.16}$$

Hence, Eqs.(A.5-7) become,

$$\frac{\partial r v_r}{\partial r} + \frac{\partial r v_z}{\partial z} = 0, \tag{A.17}$$

$$\frac{\partial(r\rho v_r)}{\partial t} + \frac{\partial(\rho r v_r)}{\partial t} + \frac{\partial(\rho r v_r^2 + pr)}{\partial r} + \frac{\partial(\rho r v_r v_z)}{\partial z} = \frac{\partial}{\partial r}(\tau_{rr}) + \frac{\partial}{\partial z}(\tau_{zr}) + p - \frac{\partial}{\partial r}(2\mu v_r) - \frac{\partial}{\partial z}(\mu v_z) - 2\mu\frac{v_r}{r}, \tag{A.18}$$

$$\frac{\partial(r\rho v_z)}{\partial t} + \frac{\partial(\rho r v_z)}{\partial t} + \frac{\partial(\rho r v_r v_z)}{\partial r} + \frac{\partial(\rho r v_z^2 + pr)}{\partial z} = \frac{\partial}{\partial r}(\tau_{zr}) + \frac{\partial}{\partial z}(\tau_{zz}) - \frac{\partial}{\partial r}(\mu v_z). \tag{A.19}$$

Equations (A.17-19) can be expressed in vector form as

$$\frac{\partial \mathbf{q}}{\partial t} + \frac{\partial \mathbf{f}}{\partial r} + \frac{\partial \mathbf{g}}{\partial z} = \frac{\partial \mathbf{f}_v}{\partial r} + \frac{\partial \mathbf{g}_v}{\partial z} + \mathbf{h}_v + \mathbf{f}_b, \tag{A.20}$$

where

$$\mathbf{q} = \begin{Bmatrix} 0 \\ r\rho v_r \\ r\rho v_z \end{Bmatrix}, \quad \mathbf{f} = \begin{Bmatrix} r v_r \\ r(\rho v_r^2 + p) \\ r\rho v_r v_z \end{Bmatrix}, \quad \mathbf{g} = \begin{Bmatrix} r v_z \\ r\rho v_r v_z \\ r(\rho v_z^2 + p) \end{Bmatrix}, \tag{A.21}$$

and

$$\mathbf{f}_v = \begin{Bmatrix} 0 \\ \tau_{rr} \\ \tau_{zr} \end{Bmatrix}, \quad \mathbf{g}_v = \begin{Bmatrix} 0 \\ \tau_{zr} \\ \tau_{zz} \end{Bmatrix}, \quad \mathbf{h}_v = \begin{Bmatrix} 0 \\ p - \frac{2}{r}\frac{\partial}{\partial r}(r\mu v_r) - \frac{\partial}{\partial z}(\mu v_z) \\ -\frac{\partial}{\partial z}(\mu v_z) \end{Bmatrix}. \tag{A.22}$$

Appendix B

ARTIFICIAL COMPRESSIBILITY PARAMETER

The artificial compressibility parameter β should be specified in such a way that it gives the best asymptotic convergence to a steady state in pseudo time. It is well known that β must be proportional to the velocity scale in convection dominated flows [29], i.e., if $Re >> 1$. An analysis is presented here to determine the optimal value of β in the Stokes' limit. In the Stokes' limit, the flow equations become

$$\begin{aligned} \nabla \cdot \mathbf{V} &= 0, \\ \nabla p - \mu \nabla^2 \mathbf{V} &= 0. \end{aligned} \tag{B.1}$$

After adding the pseudo time derivative terms, Eqs.(B.1) become

$$\begin{aligned} \frac{1}{\rho\beta^2}\frac{\partial p}{\partial \tau} &+ \nabla \cdot \mathbf{V} = 0, \\ \rho\frac{\partial \mathbf{V}}{\partial \tau} &+ \nabla p - \mu \nabla^2 \mathbf{V} = 0. \end{aligned} \tag{B.2}$$

Then taking a divergence of the momentum equation yields

$$\rho\frac{\partial}{\partial \tau}(\nabla \cdot \mathbf{V}) + \nabla^2 p - \mu \nabla^2 (\nabla \cdot \mathbf{V}) = 0. \tag{B.3}$$

Substituting the continuity equation

$$\nabla \cdot \mathbf{V} = -\frac{1}{\rho\beta^2}\frac{\partial p}{\partial \tau}, \tag{B.4}$$

into Eq.(B.2), we obtain

$$\frac{\partial^2 p}{\partial \tau^2} - \beta^2 \nabla^2 p - \nu \nabla^2 (\frac{\partial p}{\partial \tau}) = 0. \tag{B.5}$$

where $\nu = \mu/\rho$ is the kinematic viscosity. With an assumption of periodic boundary conditions, the spatial Fourier transform of Eq.(B.5) is given by

$$\frac{d^2 \hat{p}}{d\tau^2} + \nu\chi^2 \frac{d\hat{p}}{d\tau} + (\beta\chi)^2 \hat{p} = 0, \tag{B.6}$$

where $\hat{p}$ is the Fourier transform of p, $\boldsymbol{\chi}$ is the wave number vector and $\chi^2 = \boldsymbol{\chi} \cdot \boldsymbol{\chi}$. Equation(B.6) is in the same form as a mass-spring-damper system. Then looking for a solution in the form

$$\hat{p} = \hat{p}_o e^{\alpha\tau}, \tag{B.7}$$

where $\hat{p}_o$ is a function of space only, and substituting Eq.(B.7) into Eq.(B.6) yields the following characteristic equation for α

$$\alpha^2 + \nu\chi^2\alpha + (\beta\chi)^2 = 0, \tag{B.8}$$

which can be solved to get

$$\alpha_{1,2} = -\frac{\nu}{2}\chi^2 \pm \sqrt{(\frac{\nu}{2})^2\chi^4 - (\chi\beta)^2}. \tag{B.9}$$

Since $(\chi\beta)^2$ is always positive, the real parts of the both roots are negative, i.e., it is always forced to a steady state. However, the optimal damping is obtained if the terms in the square root are smaller or equal to zero, which is satisfied for

$$\beta^2 \geq \frac{1}{4}(\nu\chi)^2. \tag{B.10}$$

Now let the length scale ℓ be specified as

$$\ell = \chi_{\max}^{-1}, \tag{B.11}$$

where $\chi_{\max}$ is the maximum wavenumber, then the artificial compressibility parameter can be specified as

$$\beta^2 = \frac{1}{4}(\nu/\ell)^2 = U_{\text{ref}}^2 \frac{1}{4Re_\ell^2}, \tag{B.12}$$

where U_{ref} is a reference velocity and $Re_\ell = U_{\text{ref}}\ell/\mu$ is the Reynolds number based on U_{ref}. Combining this expression with the optimal value of β in high Reynolds number case, the artificial compressibility parameter can be specified as

$$\beta^2 = \kappa_\beta U_{\text{ref}}^2 \left(1 + \frac{1}{4Re_\ell^2}\right), \tag{B.13}$$

where κ_β is a constant of order of unity. Equation(B.13) gives a nearly optimal value for β in the entire range of Reynolds numbers although it may require to tune up the constant κ_β for some cases for the best convergence.

Appendix C

DISCRETIZATION PROCEDURE OF THE FLOW EQUATIONS

Linearization of the flow equations, the evaluation of the Jacobian matrices and discretization of the flow equations are described in detail in this Appendix. With added fourth-order artificial dissipation terms to prevent odd-even decoupling [3], Eq.(2.13) can be expressed as follows

$$\begin{aligned}\Gamma^{-1}\frac{\partial h\mathbf{w}}{\partial \tau}+\mathbf{I}^1\frac{\partial \rho h\mathbf{w}}{\partial t}+\frac{\partial h\mathbf{F}}{\partial \xi}+\frac{\partial h\mathbf{G}}{\partial \eta} &= \frac{\partial h\mathbf{F}_v}{\partial \xi}+\frac{\partial h\mathbf{G}_v}{\partial \eta}+h(\mathbf{h}_v+\mathbf{f}_b)\\ &- \Gamma^{-1}\frac{\partial}{\partial \xi}\left(\varepsilon_\xi^{(4)}h\frac{\partial^3\mathbf{w}}{\partial \xi^3}\right)-\Gamma^{-1}\frac{\partial}{\partial \eta}\left(\varepsilon_\eta^{(4)}h\frac{\partial^3\mathbf{w}}{\partial \eta^3}\right),\end{aligned} \tag{C.1}$$

where $\varepsilon_\xi^{(4)}$ and $\varepsilon_\eta^{(4)}$ are dissipation coefficients defined similar to those of Caughey [3]. The implicit scheme described in Section(2.2) to solve Eq.(C.1) can be written as

$$\begin{aligned}h\left[\frac{\Gamma^{-1}}{\Delta\tau}+I^1\frac{(2+\varphi)}{2\Delta t}\rho^{p+1}\right]\Delta\mathbf{w}^p &= -hI^1\frac{(2+\varphi)(\rho\mathbf{w})^p-2(1+\varphi)(\rho\mathbf{w})^n+\varphi(\rho\mathbf{w})^{n-1}}{2\Delta t}\\ &- \theta\left[\frac{\partial h(\mathbf{F}-\mathbf{F}_v)}{\partial \xi}+\frac{\partial h(\mathbf{G}-\mathbf{G}_v)}{\partial \eta}\right]^{p+1}+\theta h(\mathbf{h}_v^p+\mathbf{f}_b^{n+1})\\ &- \theta\left[\Gamma^{-1}\frac{\partial}{\partial \xi}\left(\varepsilon_\xi^{(4)}h\frac{\partial^3\mathbf{w}}{\partial \xi^3}\right)-\Gamma^{-1}\frac{\partial}{\partial \eta}\left(\varepsilon_\eta^{(4)}h\frac{\partial^3\mathbf{w}}{\partial \eta^3}\right)\right]^p\\ &- (1-\theta)\left[\frac{\partial h(\mathbf{F}-\mathbf{F}_v)}{\partial \xi}+\frac{\partial h(\mathbf{G}-\mathbf{G}_v)}{\partial \eta}-h(\mathbf{h}_v-\mathbf{f}_b)\right]^n\\ &- (1-\theta)\left[\Gamma^{-1}\frac{\partial}{\partial \xi}\left(\varepsilon_\xi^{(4)}h\frac{\partial^3\mathbf{w}}{\partial \xi^3}\right)+\Gamma^{-1}\frac{\partial}{\partial \eta}\left(\varepsilon_\eta^{(4)}h\frac{\partial^3\mathbf{w}}{\partial \eta^3}\right)\right]^n.\end{aligned} \tag{C.2}$$

The sub-iteration to solve Eq.(C.2) is linearized as

$$\begin{aligned}(h\mathbf{F})^{p+1} &= (h\mathbf{F})^p+A^p\Delta\mathbf{w}^p+O(\Delta\tau^2),\\ (h\mathbf{G})^{p+1} &= (h\mathbf{G})^p+B^p\Delta\mathbf{w}^p+O(\Delta\tau^2),\\ (h\mathbf{F}_v)^{p+1} &= (h\mathbf{F}_v)^p+A_v^p\Delta\mathbf{w}_\xi^p+O(\Delta\tau^2),\\ (h\mathbf{G}_v)^{p+1} &= (h\mathbf{G}_v)^p+B_v^p\Delta\mathbf{w}_\eta^p+O(\Delta\tau^2),\end{aligned} \tag{C.3}$$

where the inviscid and viscous Jacobian matrices are defined as

$$A^p = \left\{\frac{\partial h\mathbf{F}}{\partial \mathbf{w}}\right\}^p, B^p = \left\{\frac{\partial h\mathbf{G}}{\partial \mathbf{w}}\right\}^p, A_v^p = \left\{\frac{\partial h\mathbf{F}_v}{\partial \mathbf{w}_\xi}\right\}^p, B_v^p = \left\{\frac{\partial h\mathbf{G}_v}{\partial \mathbf{w}_\eta}\right\}^p, \tag{C.4}$$

with $\mathbf{w}_\xi = \frac{\partial \mathbf{w}}{\partial \xi}$ and $\mathbf{w}_\eta = \frac{\partial \mathbf{w}}{\partial \eta}$. The Jacobian matrices are explicitly given by

$$\begin{aligned}
A &= h\begin{bmatrix} 0 & 1 & 0 \\ 1 & 2\rho v_r + \frac{2\mu}{r} & 0 \\ 0 & \rho v_z & \rho v_r + \frac{\mu}{r} \end{bmatrix}, \quad B = h\begin{bmatrix} 0 & 0 & 1 \\ 0 & \rho v_z & \rho v_r + \frac{\mu}{r} \\ 1 & 0 & 2\rho v_z \end{bmatrix}, \\
A_v &= h\begin{bmatrix} 0 & 0 & 0 \\ 0 & \frac{2\mu r_\eta^2}{h^2} + \frac{\mu z_\eta^2}{h^2} & -\frac{\mu r_\eta z_\eta}{h^2} \\ 0 & -\frac{\mu r_\eta z_\eta}{h^2} & \frac{\mu r_\eta^2}{h^2} + \frac{2\mu z_\eta^2}{h^2} \end{bmatrix}, \quad B_v = h\begin{bmatrix} 0 & 0 & 0 \\ 0 & \frac{2\mu r_\xi^2}{h^2} + \frac{\mu z_\xi^2}{h^2} & -\frac{\mu r_\xi z_\xi}{h^2} \\ 0 & -\frac{\mu r_\xi z_\xi}{h^2} & \frac{\mu r_\xi^2}{h^2} + \frac{2\mu z_\xi^2}{h^2} \end{bmatrix}.
\end{aligned} \tag{C.5}$$

Using the Taylor expansions given in Eq.(C.3), the spatial derivatives are linearized as,

$$\begin{aligned}
\left(\frac{\partial h\mathbf{F}}{\partial \xi}\right)^{p+1} &= \left(\frac{\partial h\mathbf{F}}{\partial \xi}\right)^p + \frac{\partial}{\partial \xi}(A^p\Delta\mathbf{w})^p + O(\Delta\tau^2), \\
\left(\frac{\partial h\mathbf{G}}{\partial \eta}\right)^{p+1} &= \left(\frac{\partial h\mathbf{G}}{\partial \eta}\right)^p + \frac{\partial}{\partial \eta}(B^p\Delta\mathbf{w})^p + O(\Delta\tau^2), \\
\left(\frac{\partial h\mathbf{F}_v}{\partial \xi}\right)^{p+1} &= \left(\frac{\partial h\mathbf{F}_v}{\partial \xi}\right)^p + \frac{\partial}{\partial \xi}(A_v^p\Delta\mathbf{w}_\xi)^p + O(\Delta\tau^2), \\
&= \left(\frac{\partial h\mathbf{F}_v}{\partial \xi}\right)^p + \frac{\partial}{\partial \xi}\left(A_v^p\frac{\partial}{\partial \xi}\right)^p\Delta\mathbf{w}, \\
\left(\frac{\partial h\mathbf{G}_v}{\partial \eta}\right)^{p+1} &= \left(\frac{\partial h\mathbf{G}_v}{\partial \eta}\right)^p + \frac{\partial}{\partial \eta}(B_v^p\Delta\mathbf{w}_\eta)^p + O(\Delta\tau^2), \\
&= \left(\frac{\partial h\mathbf{G}_v}{\partial \eta}\right)^p + \frac{\partial}{\partial \eta}\left(B_v^p\frac{\partial}{\partial \eta}\right)^p\Delta\mathbf{w},
\end{aligned} \tag{C.6}$$

which can be substituted into Eq.(C.2) to obtain

$$\begin{aligned}
h\Big\{S + \frac{\theta}{h}\Big(\frac{\partial}{\partial \xi}A + \frac{\partial}{\partial \eta}B - \frac{\partial}{\partial \xi}A_v\frac{\partial}{\partial \xi} - \frac{\partial}{\partial \eta}B_v\frac{\partial}{\partial \eta} + \Gamma^{-1}\frac{\partial}{\partial \xi}\Big(\varepsilon_\xi^{(4)}\frac{\partial^3}{\partial \xi^3}\Big) \\
+\Gamma^{-1}\frac{\partial}{\partial \eta}\Big(\varepsilon_\eta^{(4)}\frac{\partial^3}{\partial \eta^3}\Big)\Big)\Big\}^p\Delta\mathbf{w}^p = -\mathbf{R}^p,
\end{aligned} \tag{C.7}$$

The residual vector $\mathbf{R}^p$ is composed of the physical and the numerical residuals, i.e, $\mathbf{R}^p = \mathbf{R}^p_{physical} + \mathbf{R}^p_{num,diss}$, and the physical residuals($\mathbf{R}^p_{physical}$) and numerical dissipation ($\mathbf{R}^p_{num,diss}$)

can be written explicitly as

$$\begin{aligned}\mathbf{R}^p_{physical} &= hI^1\frac{(2+\varphi)(\rho\mathbf{w})^p - 2(1+\varphi)(\rho\mathbf{w})^n + \varphi(\rho\mathbf{w})^{n-1}}{2\Delta t} \\ &+ \theta\left[\frac{\partial h(\mathbf{F}-\mathbf{F}_v)}{\partial\xi} + \frac{\partial h(\mathbf{G}-\mathbf{G}_v)}{\partial\eta} - h\mathbf{h}_v\right]^p + \theta h\mathbf{h}_b^{n+1} \\ &+ (1-\theta)\left[\frac{\partial h(\mathbf{F}-\mathbf{F}_v)}{\partial\xi} + \frac{\partial h(\mathbf{G}-\mathbf{G}_v)}{\partial\eta} - h(\mathbf{h}_v+\mathbf{f}_b)\right]^n, \end{aligned} \tag{C.8}$$

and

$$\mathbf{R}^p_{num,diss} = -\Gamma^{-1}\frac{\partial}{\partial\xi}\left(\varepsilon^{(4)}_\xi\frac{\partial^3}{\partial\xi^3}\right) - \Gamma^{-1}\frac{\partial}{\partial\eta}\left(\varepsilon^{(4)}_\eta\frac{\partial^3}{\partial\eta^3}\right), \tag{C.9}$$

Equation(C.7) is factorized following Briley and McDonald [2] and Beam and Warming [1] as follows

$$\begin{aligned} h\ &\left\{S+\frac{\theta}{h}\left(\frac{\partial}{\partial\xi}A - \frac{\partial}{\partial\xi}A_v\frac{\partial}{\partial\xi} + \Gamma^{-1}\frac{\partial}{\partial\xi}\left(\varepsilon^{(4)}_\xi\frac{\partial^3}{\partial\xi^3}\right)\right)\right\}S^{-1} \\ &\left\{S+\frac{\theta}{h}\left(\frac{\partial}{\partial\eta}B - \frac{\partial}{\partial\eta}B_v\frac{\partial}{\partial\eta} + \Gamma^{-1}\frac{\partial}{\partial\eta}\left(\varepsilon^{(4)}_\eta\frac{\partial^3}{\partial\eta^3}\right)\right)\right\}\Delta\mathbf{w}^p = -\mathbf{R}^p, \end{aligned} \tag{C.10}$$

which can be solved in two steps. In the ξ-sweep we first solve

$$\left\{S+\frac{\theta}{h}\left(\frac{\partial}{\partial\xi}A - \frac{\partial}{\partial\xi}A_v\frac{\partial}{\partial\xi} + \Gamma^{-1}\frac{\partial}{\partial\xi}\left(\varepsilon^{(4)}_\xi\frac{\partial^3}{\partial\xi^3}\right)\right)\right\}\Delta\mathbf{v}^p = -\mathbf{R}^p, \tag{C.11}$$

for the intermediate solution of $\Delta\mathbf{v}^p$ and then in η-sweep we solve

$$\left\{S+\frac{\theta}{h}\left(\frac{\partial}{\partial\eta}B - \frac{\partial}{\partial\eta}B_v\frac{\partial}{\partial\eta} + \Gamma^{-1}\frac{\partial}{\partial\eta}\left(\varepsilon^{(4)}_\eta\frac{\partial^3}{\partial\eta^3}\right)\right)\right\}\Delta\mathbf{w}^p = \frac{S\Delta\mathbf{v}^p}{h}. \tag{C.12}$$

for the corrections $\Delta\mathbf{w}^p$. Finally update the solution $\mathbf{w}^{p+1} = \mathbf{w}^p + \Delta\mathbf{w}^p$. In each sweep, a block pentadiagonal linear equation system must be solved if central differences are used to evaluate the spatial derivatives. Considering the ξ-sweep, for instance, the elements of the

pentadiagonal system are evaluated as follows

$$\frac{\partial}{\partial\xi}\left(A\Delta\mathbf{v}_{i,j}\right)^p = \frac{A_{i+1,j}\Delta\mathbf{v}_{i+1,j} - A_{i-1,j}\Delta\mathbf{v}_{i-1,j}}{2\Delta\xi} \tag{C.13}$$

$$\begin{aligned}
\frac{\partial}{\partial\xi}\left(A_v\frac{\partial}{\partial\xi}\Delta\mathbf{v}_{i,j}\right)^p &= \frac{\left(A_v\frac{\partial}{\partial\xi}\Delta\mathbf{v}\right)^p_{i+\frac{1}{2},j} - \left(A_v\frac{\partial}{\partial\xi}\Delta\mathbf{v}\right)^p_{i-\frac{1}{2},j}}{\Delta\xi} \\
&= \frac{A_{v_{i+\frac{1}{2},j}}\left(\Delta\mathbf{v}_{i+1,j} - \Delta\mathbf{v}_{i,j}\right) - A_{v_{i-\frac{1}{2},j}}\left(\Delta\mathbf{v}_{i,j} - \Delta\mathbf{v}_{i-1,j}\right)}{\Delta\xi^2} \\
&= \frac{A_{v_{i-\frac{1}{2},j}}\Delta\mathbf{v}_{i-1,j} - \left(A_{v_{i+\frac{1}{2},j}} + A_{v_{i-\frac{1}{2},j}}\right)\Delta\mathbf{v}_{i,j} + A_{v_{i+\frac{1}{2},j}}\Delta\mathbf{v}_{i+1,j}}{\Delta\xi^2} \\
&= \frac{\left(\frac{A_{v_{i,j}}+A_{v_{i-1,j}}}{2}\right)\Delta\mathbf{v}_{i-1,j} - A_{v_{i,j}}\Delta\mathbf{v}_{i,j} + \left(\frac{A_{v_{i,j}}+A_{v_{i+1,j}}}{2}\right)\Delta\mathbf{v}_{i+1,j}}{\Delta\xi^2}
\end{aligned} \tag{C.14}$$

where central differences are used to evaluate the spatial derivatives. The quantities at cell faces are evaluated as simple averages of values at cell centers, for example,

$$A_{v_{i-\frac{1}{2},j}} = \frac{1}{2}(A_{v_{i-1,j}} + A_{v_{i,j}}). \tag{C.15}$$

Similarly the artificial viscous terms are approximated as

$$\frac{\partial}{\partial\xi}\left(\varepsilon_\xi^{(4)}\frac{\partial^3}{\partial\xi^3}\right)\Delta\mathbf{v}_{i,j} = \varepsilon_\xi^{(4)}\left(\Delta\mathbf{v}_{i-2,j} - 4\Delta\mathbf{v}_{i-1,j} + 6\Delta\mathbf{v}_{i,j} - 4\Delta\mathbf{v}_{i+1,j} + \Delta\mathbf{v}_{i+2,j}\right) \tag{C.16}$$

where $\varepsilon_\xi^{(4)}$ is taken as constant. Substituting Eqs.(C.13-16) into Eq.(C.11) with $\Delta\xi = 1$, $\Delta\eta = 1$ yields the following block pentadiagonal system of equations,

$$\begin{aligned}
&\frac{\theta}{h}\left[\frac{A_{i+1,j}\Delta\mathbf{v}_{i+1,j} - A_{i-1,j}\Delta\mathbf{v}_{i-1,j}}{2}\right] \\
-\ &\frac{\theta}{h}\left[\left(\frac{A_{v_{i,j}} + A_{v_{i-1,j}}}{2}\right)\Delta\mathbf{v}_{i-1,j} - A_{v_{i,j}}\Delta\mathbf{v}_{i,j} + \left(\frac{A_{v_{i,j}} + A_{v_{i+1,j}}}{2}\right)\Delta\mathbf{v}_{i+1,j}\right] \\
+\ &\frac{\theta}{h}\left[\Gamma^{-1}\varepsilon_\xi^{(4)}\left(\Delta\mathbf{v}_{i-2,j} - 4\Delta\mathbf{v}_{i-1,j} + 6\Delta\mathbf{v}_{i,j} - 4\Delta\mathbf{v}_{i+1,j} + \Delta\mathbf{v}_{i+2,j}\right)\right] \\
+\ &S\Delta\mathbf{v}_{i,j} = -\mathbf{R}
\end{aligned} \tag{C.17}$$

which can be written in a compact form as

$$\mathbf{duu}\Delta\mathbf{v}_{i-2,j} + \mathbf{du}\Delta\mathbf{v}_{i-1,j} + \mathbf{dd}\Delta\mathbf{v}_{i,j} + \mathbf{dl}\Delta\mathbf{v}_{i+1,j} + \mathbf{dll}\Delta\mathbf{v}_{i+2,j} = \mathbf{R}_{i,j}, \tag{C.18}$$

where

$$\begin{aligned}
\mathbf{duu} &= \frac{\Gamma^{-1}\theta\varepsilon_{\xi}^{(4)}}{h}, \\
\mathbf{du} &= \frac{\theta}{h}\left[-\frac{A_{i-1,j}}{2} - \frac{A_{v_{i,j}} + A_{v_{i-1,j}}}{2} - 4\Gamma^{-1}\varepsilon_{\xi}^{(4)}\right], \\
\mathbf{dd} &= \frac{\theta}{h}\left[S + \frac{A_{v_{i,j}}}{2} + 6\Gamma^{-1}\varepsilon_{\xi}^{(4)}\right], \\
\mathbf{dl} &= \frac{\theta}{h}\left[\frac{A_{i+1,j}}{2} - \frac{A_{v_{i,j}} + A_{v_{i+1,j}}}{2} - 4\Gamma^{-1}\varepsilon_{\xi}^{(4)}\right], \\
\mathbf{dll} &= \frac{\Gamma^{-1}\theta\varepsilon_{\xi}^{(4)}}{h}.
\end{aligned} \tag{C.19}$$

Note that **duu, du, dd, dl, dll** are 3×3 matrices. Similarly in η direction the pentadiagonal system of equations is given by

$$\mathbf{duu}\Delta\mathbf{w}_{i-2,j} + \mathbf{du}\Delta\mathbf{w}_{i-1,j} + \mathbf{dd}\Delta\mathbf{w}_{i,j} + \mathbf{dl}\Delta\mathbf{w}_{i+1,j} + \mathbf{dll}\Delta\mathbf{w}_{i+2,j} = (\frac{S\Delta\mathbf{v}}{h})_{i,j}, \tag{C.20}$$

where,

$$\begin{aligned}
\mathbf{duu} &= \frac{\Gamma^{-1}\theta\varepsilon_{\eta}^{(4)}}{h}, \\
\mathbf{du} &= \frac{\theta}{h}\left[-\frac{B_{i-1,j}}{2} - \frac{B_{v_{i,j}} + B_{v_{i-1,j}}}{2} - 4\Gamma^{-1}\varepsilon_{\eta}^{(4)}\right], \\
\mathbf{dd} &= \frac{\theta}{h}\left[S + \frac{B_{v_{i,j}}}{2} + 6\Gamma^{-1}\varepsilon_{\eta}^{(4)}\right], \\
\mathbf{dl} &= \frac{\theta}{h}\left[\frac{B_{i+1,j}}{2} - \frac{B_{v_{i,j}} + B_{v_{i+1,j}}}{2} - 4\Gamma^{-1}\varepsilon_{\eta}^{(4)}\right], \\
\mathbf{dll} &= \frac{\Gamma^{-1}\theta\varepsilon_{\eta}^{(4)}}{h}.
\end{aligned} \tag{C.21}$$

BIBLIOGRAPHY

[1] R.M. Beam and R.F. Warming, "An implicit factored scheme for the compressible Navier-Stokes equations," *AIAA J.*, vol. 16, pp. 393–402, 1978.

[2] W.R. Briley and H. McDonald, "Solution of the tree-dimensional compressible Navier-Stokes equations by an implicit technique," *Lecture Notes in Physics*, vol. 35, pp. 105–10, New York:Verlag, 1974.

[3] D.A. Caughey, "Diagonal implicit multigrid algorithm for the Euler equations," *AIAA J.*, vol. 26, pp. 841–851, 1988.

[4] D.A.Caughey, "Implicit multigrid computation of unsteady flows past cylinders of square cross-section," *Computers&Fluids*, vol. 30, pp. 940–960, 2001.

[5] J.H. Che, "Numerical simulation of multiphase flows: Electrohydrodynamics and solidification of droplets," *Ph.D. Thesis*, The University of Michigan, Ann Arbor, 1999.

[6] L. Fauci and S. Gueron, Eds. *Computational modeling in biological fluid dynamics*, Springer-Verlag, New York, 2001.

[7] J. Han and G. Tryggvason, "Secondary breakup of axisymmetric liquid drops: I. Acceleration by a constant body force," *Phys. Fluids*, vol. 11(12), pp. 3650–3667, 1999.

[8] M. Hemmat and A. Borhan, "Buoyancy-driven motion of drops and bubbles in a periodically constricted capillary," *Chem. Eng. Commun.*, vol. 150, pp. 363–384, 1996.

[9] C.W. Hirt and B.D. Nichols, "Volume of fluid (VOF) method for the dynamics of free boundaries," *J. Comput. Phys.*, vol. 39, pp. 201–225, 1981.

[10] C.W. Hirt, A.A. Amsden and J.L. Cook, "An arbitrary Lagrangian-Eulerian computing method for all flow speeds," *J. Comput. Phys.*, vol. 135, pp.203–216, 1997.

[11] K.A. Hoffmann and S.T. Chiang, *Computational Fluid Dynamics Volume I*, Engineering Education System, Wichita, 1998.

[12] M. Muradoglu and A.D. Kayaalp, "A Finite-Volume/Front-Tracking Method for Computations of Multiphase Flows in Complex Geometries," *J.Comput. Phys*, submitted, 2004.

[13] H. Lamb, *Hydrodynamics*, Dover Publishers, New York, 1932.

[14] M. Manga, "Dynamics of Droplets in branched tubes," *J. Fluid Mech.*, vol. 315, pp. 105–117, 1996.

[15] M. Muradoglu, P. Jenny, S.B. Pope and D.A. Caughey, "A consistent hybrid finite-volume/particle method for the PDF equations of turbulent reactive flows," *J. Comput. Phys.*, vol. 154(2), pp.342–371, 1999.

[16] M. Muradoglu and S. Gokaltun, "Implicit multigrid computations of buoyant light drops through sinusoidal constrictions," *ASME J. Applied Mech.*, in press, 2004.

[17] W.L. Olbricht and L.G. Leal, "The creeping motion of immiscible drops through a converging/diverging tube," *J. Fluid Mech.*, vol. 134, pp. 329–355, 1983.

[18] W.L. Olbricht, "Pore-scale prototypes of multiphase flow in porous media," *Annu. Rev. Fluid Mech.*, vol. 28, pp. 187–213, 1996.

[19] S. Osher and R.P. Fedkiw, "Level set methods: An overview," *J. Comput. Phys.*, vol. 169(2), pp. 463–502, 2001.

[20] C. Peskin, "Numerical analysis of blood flow in the heart," *J. Comput. Phys.*, vol. 25, pp. 220–252, 1977.

[21] C. Pozrikidis, Ed. *Modeling and simulation of capsules and biological cells*, Chapman&Hall/CRC, 2003.

[22] T.H. Pulliam and D.S. Chaussee, "A diagonal form of an implicit approximate factorization algorithm," *J. Comput. Phys.*, vol. 39, pp. 347–363, 1981.

[23] G. Ryskin and L.G. Leal, "Numerical simulation of free-boundary problems in fluid mechanics, Part 2. Buoyancy-driven motion of a gas bubble through a quiescent liquid," *J. Fluid Mech.*, vol. 148, pp.19–35, 1984.

[24] R. Scardovelli and S. Zaleski, "Direct numerical simulation of free-surface and interfacial flow," *Annu. Rev. Fluid Mech.*, vol. 31, pp. 567–603, 1999.

[25] J.A. Sethian and P. Smereka, "Level set methods for fluid interfaces," *Annu. Rev. Fluid Mech.*, vol. 35, pp. 341– , 2003.

[26] H.A. Stone, A.D. Stroock and A. Ajdary, "Engineering flows in small devices: Microfluidics toward lab-on-a-chip," *Annu. Rev. Fluid Mech.*, vol. 36, pp. 381–411, 2004.

[27] M. Sussman, P. Smereka and S. Osher, "A level set approach for computing solutions to incompressible two-phase flows," *J. Comput. Phys.*, vol. 114, pp. 146–159, 1999.

[28] G. Tryggvason, B. Bunner, A. Esmaeeli, D. Juric, N. Al-Rawahi, W. Tauber, J. Han, S. Nas and Y.-J. Jan, "A Front-Tracking Method for the Computations of Multiphase Flow," *J. Comput. Phys.*, vol. 169(2), pp. 708–759, 2001.

[29] E. Turkel, "Preconditioning methods for solving incompressible and low speed compressible flows," *J. Comput. Phys.*, vol. 72, pp. 277–298, 1987.

[30] T.M. Tsai, M.J. Miksis, "Dynamics of a droplet in a constricted capillary tube," *J. Fluid Mech.*, vol. 274, pp. 197–217, 1994.

[31] H.S. Udaykumar, H.-C. Kan, W. Shyy and R. Tran-Son-Tay, "Multiphase dynamics in arbitrary geometries on fixed Cartesian grids," *J. Comput. Phys.*, vol. 137, pp. 366–405, 1997.

[32] S.O. Unverdi and G. Tryggvason, "A front-tracking method for viscous incompressible multiphase flows," *J. Comput. Phys.*, vol. 100, pp. 25–37, 1992.

[33] T. Yabe, F. Xiao and T. Utsumi, "The constrained interpolation profile (CIP) method for multiphase analysis," *J. Comput. Phys.*, vol. 169(2), pp. 556–593, 2001.

VITA

Arif Doruk Kayaalp was born in Istanbul, Turkey on July 1, 1980 . He completed the high school in Üsküdar American Academy, Istanbul, in 1998. He received the B. Sc. degree in Mechanical Engineering from Boğaziçi University, Istanbul, in 2002. In October 2002, he joined to the Mechanical Engineering Department of Koç University, Istanbul, Turkey as a teaching and research assistant and had studied for the *"A Finite-Volume/Front-Tracking Method for Computations of Multiphase Flows in Complex Geometries"* project since October 2002.